2016

Studies Of Asphalt Roofing Sealant Failure For Shingle Systems Subjected To High Wind Conditions For Both Elastic And Viscoelastic Sealant Material Response

Artem Aleshin
University of South Carolina

STUDIES OF ASPHALT ROOFING SEALANT FAILURE FOR SHINGLE SYSTEMS SUBJECTED TO HIGH WIND CONDITIONS FOR BOTH ELASTIC AND VISCOELASTIC SEALANT MATERIAL RESPONSE

by

Artem Aleshin

Bachelor of Science
University of South Carolina, 2014

Submitted in Partial Fulfillment of the Requirements

For the Degree of Master of Science in

Mechanical Engineering

College of Engineering and Computing

University of South Carolina

2016

Accepted by:

Michael Sutton, Director of Thesis

Fabio Matta, Reader

Lacy Ford, Senior Vice Provost and Dean of Graduate Studies

DEDICATION

To my parents, Yuriy and Svetlana, my sister, Polina, my grandparents, Yevgeny, Anatoly, Valentina and Tamara, as well as Jessica, whose support I greatly appreciate, and of course, Billy and Sheila, all of who encouraged me and have shaped my path in this life.

ACKNOWLEDGEMENTS

The support of the Department of Mechanical Engineering at the University of South Carolina, especially through its purchase of the specialized TA compression fixtures for the RSA III Viscoelastic Property determination system, is gratefully acknowledged. The assistance of Mr. Bill Bradley, who created the mold necessary for the manufacturing of bitumen specimens is deeply appreciated. The assistance of Mr. Brendan Croom, who provided me a complete and functional copy of the original Python-based software for the sealant analyses performed by him for the single sealant system, is deeply appreciated. The assistance of Prof. Fabio Matta in reviewing and modifying the first several chapters of this thesis is appreciated and gratefully acknowledged. Finally, the support of Prof. Michael Sutton throughout this research effort is deeply appreciated.

ABSTRACT

It has been documented that the sealant between asphalt roof shingles may delaminate at significantly lower wind speeds than those for which they are rated, with major consequences on safety and repair costs. In perspective, developing more resilient material systems and devising more effective installation procedures are sensible strategies to mitigate this problem. A practical approach may also entail adding a second self-sealing strip. In the first portion of this thesis, the elastic structural response of an asphalt roof shingle-sealant system consisting of individual three-tab shingles, which are bonded to the underlying shingles with two sealant strips and are subjected to uplift pressures that are produced by high wind loads, is simulated using a beam-on-elastic foundation (BOEF) model. The introduction of an additional sealant strip compared to conventional one-strip configurations is investigated to understand the effectiveness in resisting high wind loads (*e.g.*, Category 4 hurricanes). Specifically, the two-sealant strip BOEF model is used to (a) estimate the applied energy release rate, G, along the edges of each sealant strip and (b) study the influence of sealant strips location and out-of-plane stiffness. It is found that standard three-tab shingles can be designed to optimize the position of two sealant strips, resulting in maximum G values that are approximately fourteen times smaller than those in conventional (one-sealant strip) counterparts. In addition, the maximum G values are far less sensitive to changes in sealant stiffness. The results of this study suggest that, from a mechanical standpoint, the addition of a second self-sealing strip is an efficient means to radically increase resiliency against high wind loads, and offset detrimental aging effects.

Since the sealant material is a form of bitumen, it is well known that such materials exhibit viscoelastic behavior when subjected to mechanical loads over an extended period of time. Thus, if the sealant system used in an application does not fail elastically during the early stages of loading, then its ability to sustain prolonged mechanical loading over an extended period of time without failure must be considered. This is particularly true for shingle systems when subjected to hurricane force winds that may last for several hours. Thus, the second portion of this thesis addresses the time-dependent response of the sealant material used in asphalt shingles. The viscoelastic properties of the sealant material were characterized through several creep compression tests and the use of Time-Temperature Superposition principles. The resulting viscoelastic properties were then used to create finite element analysis models in order to simulate the transient response of single and double sealant asphalt shingle structures subjected to uplift pressure loading that they would encounter during Category 4 hurricanes. Using beam elements on a viscoelastic foundation to perform simulations, it was determined that single sealant asphalt shingles will fail somewhere in between 4.1 and 4.3 hours when subjected to expected pressure loading conditions, while shingles with two sealant strips will require far more than 5 hours to approach failure conditions.

PREFACE

Chapters 1 through 5 of this thesis address the problem of a double self-sealant strip asphalt shingle subjected to quasi-static pressure loading. Chapters 6 through 11 address the problems of viscoelasticity and the transient responses of single and double self-sealant strip asphalt shingles when subjected to pressure loading for an extended period of time. Every effort has been made to provide sufficient information so that the results presented in this thesis can be replicated (perhaps even more effectively) by anyone who wishes to put forth the time and thought necessary to complete the work.

TABLE OF CONTENTS

DEDICATION iii

ACKNOWLEDGEMENTS iv

ABSTRACT v

PREFACE vii

LIST OF TABLES x

LIST OF FIGURES xi

CHAPTER 1: INTRODUCTION TO MODELING OF DOUBLE SEALANT SYSTEMS 1

CHAPTER 2 ANALYTICAL MODEL OF SHINGLE-SEALANT STRUCTURE 4

2.1 MATHEMATICAL FORMULATION 5

2.2 SHINGLE-SEALANT BOND ENERGY RELEASE RATE 7

CHAPTER 3 PARAMETRIC STUDY OF SHINGLE-SEALANT STRUCTURAL RESPONSE 11

3.1 ASSUMPTIONS AND LIMITATIONS OF MECHANICAL MODEL 12

CHAPTER 4 RESULTS AND DISCUSSIONS OF PARAMETRIC STUDIES 14

4.1 INFLUENCE OF SEALANT STRIP LOCATION ON APPLIED *G* AT SEALANT STRIP EDGES 14

4.2 COMPARISON WITH STANDARD ASPHALT-SHINGLE SYSTEM WITH ONE SEALANT STRIP 17

4.3 INFLUENCE OF SEALANT STIFFNESS ON APPLIED *G* AT SEALANT STRIP EDGES 18

CHAPTER 5 CONCLUSIONS TO MODELING OF DOUBLE SEALANT SYSTEMS.....24

CHAPTER 6 INTRODUCTION TO SEALANT CHARACTERIZATION AND MODELING OF SEALANT EXHIBITING VISCOELASTIC RESPONSE.....26

CHAPTER 7 THEORETICAL BACKGROUND.....28

7.1 DERIVATION OF VISCOELASTIC CREEP LAW.....28

7.2 DERIVATION OF VISCOELASTIC CONSTANTS.....29

7.3 SHINGLE-SEALANT FAILURE MODELS AND BOND ENERGY RELEASE RATE.....30

CHAPTER 8 CHARACTERIZATION OF SEALANT MATERIAL.....32

8.1 MANUFACTURING OF SPECIMENS.....32

8.2 UNIAXIAL COMPRESSION TEST AND THE YOUNG'S MODULUS OF THE SEALANT MATERIAL.....33

8.3 UNIAXIAL COMPRESSION CREEP TESTS.....34

8.4 TIME-TEMPERATURE SUPERPOSITION.....34

8.5 VISCOELASTIC ENERGY RELEASE RATE.....36

8.6 RELAXED MODULUS AND YOUNG'S MODULUS OF SECOND LINEAR ELASTIC DAMPER.....37

8.7 EFFECTIVE EXTENSIONAL VISCOSITY.....37

CHAPTER 9 FINITE ELEMENT ANALYSIS STUDIES OF SHINGLE-SEALANT STRUCTURAL RESPONSE.....50

CHAPTER 10 RESULTS AND DISCUSSIONS OF VISCOELASTIC SIMULATIONS.....60

CHAPTER 11 CONCLUSIONS TO SEALANT CHARACTERIZATION AND VISCOELASTIC SIMULATIONS.....67

CHAPTER 12 LIMITATIONS OF CURRENT STUDIES AND FUTURE WORK.....69

REFERENCES.....71

LIST OF TABLES

Table 2.1 Asphalt roof shingle-sealant structural model parameters and dimensional units. 8

Table 2.2 Model boundary conditions and continuity equations. 9

Table 4.1 Simulation results for G_{min} and corresponding l_1 (distance between nail line and inner edge of inner sealant strip) for fixed l_5 (shingle lip length). 19

Table 4.2 Simulation results for G_{min} and corresponding l_1 (distance between nail line and inner edge of inner sealant strip) for fixed S (sealant elastic stiffness parameter). 19

Table 8.1 Dimensions of shingle sealant material specimens used for testing. 38

Table 8.2 Values of the logarithm of the shift factor at various testing temperatures. 38

Table 8.3 Properties of shingle sealant material computed from experimental data. 38

Table 9.1 Asphalt roof shingle-sealant FEA model parameters and dimensional units. ... 54

Table 9.2 Dimensions of Models S1 and S2. 56

Table 9.3 Dimensions of Models D1 and D2. 56

Table 9.4 Element (BEAM189) and node counts of FEA models. 57

Table 9.5 Forces applied to single and double sealant FEA models. 57

Table 10.1 Final values of G at the edges of the sealant in Models S1 and S2. 62

Table 10.2 Final values of G at the edges of the sealants in Models D1 and D2. 62

LIST OF FIGURES

Figure 1.1 Photograph of mock-up asphalt roof shingle with one self-sealing adhesive strip. 3

Figure 2.1 Structural model: (a) schematic of asphalt roof shingle-sealant system; and (b) loading and boundary conditions. Note that axis *z* is perpendicular to axis *x* and *y*.....10

Figure 3.1 Structural model used in parametric study, with $p_1 = p_3 = 507$ Pa and $p_5 = 2028$ Pa, after Peterka et al. (1997).....13

Figure 4.1 Applied *G* at sealant strip edges as function of clear spacing between sealant strips (l_3 in Figure 3.1), *i.e.*, by varying l_1 for constant sealant strip length ($l_2 = l_4 = 0.0127$ m), shingle lip length ($l_5 = 0.00154$ m), and total shingle tab length ($l_1 + l_2 + l_3 + l_4 + l_5 = 0.1334$ m): (a) inner and outer edge of inner sealant strip; and (b) inner and outer edge of outer sealant strip. 20

Figure 4.2 Applied *G* at sealant strip edges as function of clear spacing between sealant strips (l_3 in Figure 3.1), *i.e.*, by varying l_1 for constant sealant strip length ($l_2 = l_4 = 0.0127$ m), shingle lip length ($l_5 = 0$ m), and total shingle tab length ($l_1 + l_2 + l_3 + l_4 + l_5 = 0.1334$ m): (a) inner and outer edge of inner sealant strip; and (b) inner and outer edge of outer sealant strip. 21

Figure 4.3 Applied *G* at sealant strip edges as function of clear spacing between sealant strips (l_3 in Figure 3.1), *i.e.*, by varying l_1 for constant sealant strip length ($l_2 = l_4 = 0.0127$ m), shingle lip length ($l_5 = 0.008$ m), and total shingle tab length ($l_1 + l_2 + l_3 + l_4 + l_5 = 0.1334$ m). Note minimized $G_{\min} = 0.034$ J/m^2 for $l_1 = 0.052$ m. 22

Figure 4.4 Applied *G* at all sealant strip edges for selected shingle lip length (l_5) values, and associated $G_{\min}$ for optimal configuration (consistent with simulation results and l_1 values in Table 4.1)....34 Figure 1.1 Photograph of mock-up asphalt roof shingle with one self-sealing adhesive strip. 23

Figure 7.1 Standard Linear Solid model comprised of a linear damper with modulus E_1 in series with a Kelvin-Voigt unit comprised of a linear damper with modulus E_2 and a dashpot with an effective extensional viscosity of η_e.....31

Figure 8.1 Stainless steel mold used for manufacturing specimens from shingle sealant material in: (a) disassembled form; and (b) assembled form. Ruler units in centimeters. 39

Figure 8.2 Shingle sealant material Specimen 1: (a) front view; and (b) side view. Ruler units in centimeters. 39

Figure 8.3 Cylindrical specimen composed of sealant strip material in between steel platens of RSA III test system. As the specimen is compressed, the diameter of the specimen grows outward towards the edges of the platens. Ruler units in centimeters. ...40

Figure 8.4 Experimental compressive stress-strain response of sealant specimen shown in Figure 8.2 (obtained at temperature of 23°C). 40

Figure 8.5 (a) True compressive stress response; and (b) true compressive strain response, as a function of time, of Specimens 2-6 loaded with a constant compressive stress of 23,735 Pa at temperatures of 23, 28, 33, 38 and 43ºC respectively.....41

Figure 8.6 (a) True compressive stress response; and (b) true compressive strain response, as a function of logarithmic time, of Specimens 2-6 loaded with a constant compressive stress of 23,735 Pa at temperatures of 23, 28, 33, 38 and 43ºC, respectively. 42

Figure 8.7 TTSP shifts of true compressive strain data from (a) 28 to 23ºC; (b) 33ºC to the 23ºC data extended by the shift of 28ºC data; (c) 38ºC to the 23ºC data extended by the shift of 28 and 33ºC data; (d) 43ºC to the 23ºC data extended by the shift of 28, 33 and 43ºC data. 43

Figure 8.8 True compressive (a) stress; and (b) strain; response of shingle sealant material at 23ºC and under a constant compressive stress of 23,735 Pa after TTSP as functions of logarithmic time. 45

Figure 8.9 True compressive (a) stress; and (b) strain; response of shingle sealant material at 23ºC and under a constant compressive stress of 23,735 Pa after TTSP. 46

Figure 8.10 Plot of $-1/\log a_T$ as a function of $1/(T - T_{ref})$ as well as the linear regression line used for the calculation of WLF constants D_1 and D_2, as per **Eq. (13)**. Functional fit is written y = -18.917x + 0.7856. 47

Figure 8.11 True compressive stress-strain data (obtained from the combination of data in Figure 8.9) and second order polynomial fit. Functional fit is written $y = 16.690x^2 + 22.550x + 23.735$ with $R^2 = 1.000$ 48

Figure 8.12 Effective extensional viscosity of shingle sealant material over the course of: (a) 5 hours with polynomial fit $y = 6.50E{+}06x^6 - 1.18E{+}08x^5 + 8.50E{+}08x^4 - 2.95E{+}09x^3 + 4.51E{+}09x^2 - 1.40E{+}08x + 1.00E{+}09$ and $R^2 = 1.00E{+}00$; and (b) 92,477 hours with $y = 1.16E{-}15x^6 - 3.05E{-}10x^5 + 3.37E{-}05x^4 - 3.16E{+}00x^3 + 2.88E{+}05x^2 + 1.28E{+}09x + 1.00E{+}09$ and $R^2 = 1.00E{+}00$. 49

Figure 9.1 Structural model with loading and boundary conditions of (a) single sealant asphalt roof shingle-sealant system; and (b) double sealant asphalt roof shingle-sealant system. Note that axis *z* is perpendicular to axis *x* and *y* and springs denote a viscoelastic foundation. 58

Figure 9.2 Meshed geometries of single sealant Models S1 and S2 made up of Regions 1s (composed of e_1^s BEAM189 elements), 2s (composed of e_2^s BEAM189 elements and n_2^s LINK180 elements) and 3s (composed of e_3^s BEAM189 elements). The quantities of elements in each region are located in Table 9.4. 59

Figure 9.3 Meshed geometries of double sealant Models D1 and D2 made up of Regions 1d (composed of e_1^d BEAM189 elements), 2d (composed of e_2^d BEAM189 elements and n_2^s LINK180 elements), 3d (composed of e_3^d BEAM189 elements), 4d (composed of e_4^d BEAM189 elements and n_2^s LINK180 elements) and 5d (composed of e_5^d BEAM189 elements). The quantities of elements in each region are located in Table 9.4. 59

Figure 10.1 Applied energy release rate, *G*, at the inner and outer edges of the sealant for the duration of the simulations in (a) single sealant Model S1; and (b) single sealant Model S2. 63

Figure 10.2 (a) Stress; and (b) strain distributions in the y-direction (Figure 9.1a) in the sealant of single sealant Model S1. 64

Figure 10.3 Applied energy release rate, *G*, at the inner edge of the inner sealant, the outer edge of the inner sealant, the inner edge of the inner sealant and the outer edge of the outer sealant for the duration of the simulations in (a) double sealant Model D1; and (b) double sealant Model D2.....65

Figure 10.4 Maximum applied energy release rate, *G*, for the duration of simulations of Models S1, S2, D1 and D2, and the lower and upper bounds of the critical viscoelastic energy release rate, G_c.....66

CHAPTER 1

INTRODUCTION TO MODELING OF DOUBLE SEALANT SYSTEMS

Modern one-layer asphalt roof shingles typically consist of fiber-reinforced laminates that contain a chemical saturant to ensure sufficient fire resistance (Dixon et al. 2012). One self-sealing strip is used to adhesively bond the top shingle to the one beneath (Figure 1.1), thereby minimizing water penetration and providing uplift resistance. Self-sealing strips are typically made of limestone- or fly ash-modified resins, or polymer-modified bitumen, to provide endurance against embrittlement due to aging, especially as a result of thermal effects (Shiao et al. 2003a). However, it has been reported that recently installed asphalt shingles that were rated for resistance against 177-km/h to 241-km/h 3-s gusts (ASTM 2009, 2011) delaminated when subject to 185-km/h or less 3-s gusts produced by Hurricane Ike (Liu et al. 2010). Durability is also of concern as resistance can be impaired by aging effects (Dixon et al. 2014a, 2014b).

While research is ongoing to develop standard test methods to realistically simulate high wind loads for shingle rating (*e.g.*, Ghorbani et al. 2015), mitigating this problem may call for the development of more resilient material systems, and perhaps the definition of more effective installation procedures. From a mechanical standpoint, a practical option consists in adding a second self-sealing strip. This strategy would become more attractive if it led to a radical enhancement in shingle uplift resistance and durability, possibly justifying the additional materials and manufacturing cost. To this end, it is noted that

shingle delamination often results in water intrusion, with interior losses that can be nine times higher in cost than those to the building envelope (Sparks et al. 1994).

Recently, Croom et al. (2015a, 2015b) introduced a beam-on-elastic-foundation (BOEF) model to simulate the uplift response of conventional asphalt roof shingle-sealant structures with a single sealant strip. This model was used in numerical simulations to study the influence of salient geometric parameters (*e.g.*, sealant strip size and position) and material properties (*e.g.*, sealant out-of-plane stiffness). It was found that: (a) modern shingle systems are approximately optimized to resist uplift pressures produced under high winds; and (b) uplift pressures produced under 150-mph winds can induce delamination of typical asphalt roof shingles.

In this thesis, this mechanical model is modified to include two sealant strips and then used to: (a) study trends in the applied energy release rate, G, at both edges of each sealant strip as a function of sealant strips location, sealant stiffness, and uplift pressures on the shingle for a 150-mph 3-s gust; (b) determine the placement of both sealant strips that enables one to minimize the applied energy release rate for the sealant strip edge subject to the maximum separation forces, that is, to maximize the life of the shingle with the given engineering constraints; and (c) compare optimized two-sealant strip and conventional one-sealant strip designs (Figure 1.1) based on their maximum G, as determined by Croom et al. (2015b) for the latter, to quantify the significance of adding a second sealant strip.

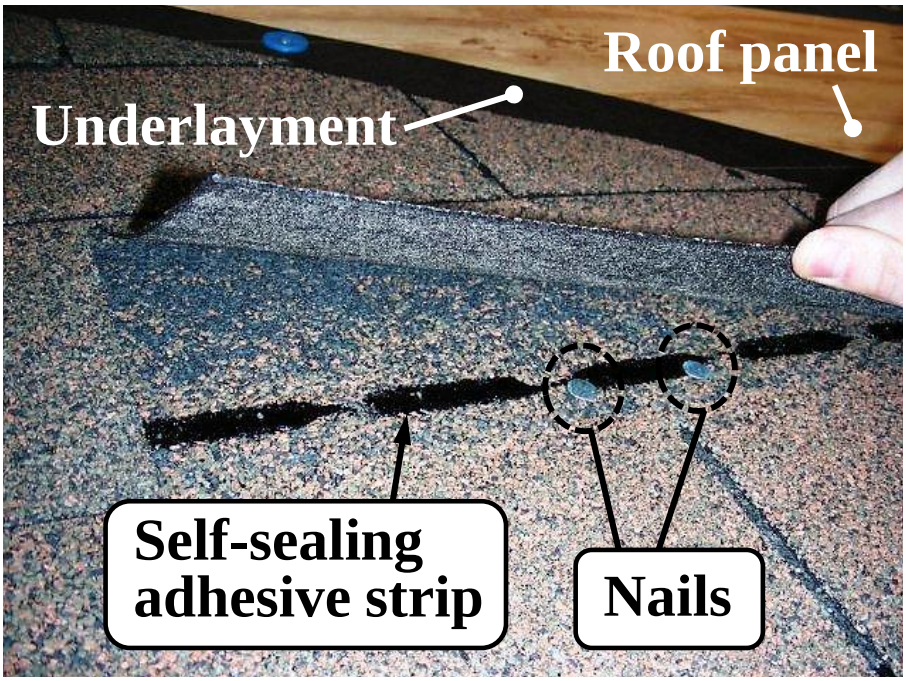

Figure 1.1 Photograph of mock-up asphalt roof shingle with one self-sealing adhesive strip.

CHAPTER 2

ANALYTICAL MODEL OF SHINGLE-SEALANT STRUCTURE

A schematic of a one-layer asphalt roof shingle system that is modified to include two adhesive sealant strips is shown in Figure 2.1a. The associated BOEF mechanical model is illustrated in Figure 2.1b where the nail line is approximated as a fixed end. It is assumed that (Croom et al. 2015a): (a) a "unit width" in the *z*-direction (orthogonal to *x* and *y* in Figure 2.1) experiences a uniform response; and (b) adhesive sealant strips have a uniform width along their entire length, that is, the gaps found in "intermittent" strips (Figure 1.1) are not specifically modeled.

Table 2.1 provides a list of the BOEF model parameters, notations, and dimensional units as used in this paper. As illustrated in Figure 2.1b, the shingle of length $l = l_1 + l_2 + l_3 + l_4 + l_5$ is modeled as a beam with flexural stiffness EI, and the inner and outer sealant strips having length l_2 and l_4, respectively, are modeled as elastic foundations having similar axial stiffness, S. The constant uplift pressures p_1 and p_3 applied between the nail line and the inner edge of the inner sealant strip, and between the outer edge of the inner sealant strip and the inner edge of the outer sealant strip, respectively, are assumed to be independent loading parameters over the lengths l_1 and l_3, respectively, on the shingle. It is noted that while line loads (units FL^{-1}) are typically used in beam problems, pressure loads (units FL^{-2}) are used in this paper to ensure consistency with uplift pressure values; a beam with unit width of 1 m is assumed, which makes these two load types functionally equivalent based on the relation *line load* = *pressure* × *width*. In the mechanical model,

both the location and length of each sealant strip along the shingle edge (axis x) can be varied to quantify their influence on the resistance to delamination.

2.1 MATHEMATICAL FORMULATION

Based on Euler-Bernoulli beam theory, the out-of-plane deflection (y-direction in Figure 2.1) of the shingle is modeled based on the formulation presented in **Eq. (1)**.

$$EI\frac{\partial^4 w_i}{\partial x^4} = F_i\left(x\right),\quad F_i\left(x\right) = \begin{cases} p_i\left(x\right) & \text{for } i = 1,3,5 \\ -Sw_i\left(x\right) & \text{for } i = 2,4 \end{cases} \tag{1}$$

The analytical solutions for the deflections $w_i(x)$ in **Eq. (1)** where i = 1, 2, 3, 4 and 5 is associated with Region 1, 2, 3, 4 and 5, respectively, along the shingle (Figure 2.1), can be expressed by means of **Eq. (2)** through **Eq. (6)**:

$$w_1\left(x\right) = \frac{1}{EI}\left(C_1 + C_2 x + \frac{C_3 x^2}{2} + \frac{C_4 x^3}{6} + \frac{p_1 x^4}{24}\right) \tag{2}$$

$$w_2\left(x\right) = C_5 e^{\alpha x}\cos\left(\alpha x\right) + C_6 e^{\alpha x}\sin\left(\alpha x\right) + C_7 e^{-\alpha x}\cos\left(\alpha x\right) + C_8 e^{-\alpha x}\sin\left(\alpha x\right) \tag{3}$$

$$w_3\left(x\right) = \frac{1}{EI}\left(C_9 + C_{10} x + \frac{C_{11} x^2}{2} + \frac{C_{12} x^3}{6} + \frac{p_3 x^4}{24}\right) \tag{4}$$

$$w_4\left(x\right) = C_{13} e^{\alpha x}\cos\left(\alpha x\right) + C_{14} e^{\alpha x}\sin\left(\alpha x\right) + C_{15} e^{-\alpha x}\cos\left(\alpha x\right) + C_{16} e^{-\alpha x}\sin\left(\alpha x\right) \tag{5}$$

$$w_5\left(x\right) = \frac{1}{EI}\left(C_{17} + C_{18} x + \frac{C_{19} x^2}{2} + \frac{C_{20} x^3}{6} + \frac{p_5 x^4}{24}\right) \tag{6}$$

where the parameter α is equal to $(S/EI)^{0.25}$. The boundary conditions at $x = 0$, $x = l_1$, $x = l_1 + l_2$, $x = l_1 + l_2 + l_3$, $x = l_1 + l_2 + l_3 + l_4$ (Figure 2.2) are presented in Table 2.2. It is assumed that the uplift displacement and uplift slope at the nail section (x = 0) are equal to zero,

thereby representing a fixed support. These continuity equations are then used in conjunction with the static equilibrium equations in **Eq. (7)** and **Eq. (8)** to calculate the values for the reaction bending moment and shear force (M_w and V_w at x = 0), and the constants of integration in **Eq. (2)** and **Eq. (6)** (C_1 through C_{20}).

$$\sum M_z\left(x=0\right)$$
$$M_w-\int_0^{l_1} p_1\left(x\right)x\,dx+\int_{l_1}^{l_1+l_2} w_2\left(x\right)S\;x\,dx-\int_{l_1+l_2}^{l_1+l_2+l_3} p_3\left(x\right)x\,dx$$
$$+\int_{l_1+l_2+l_3}^{l_1+l_2+l_3+l_4} w_4\left(x\right)S\;x\,dx-\int_{l_1+l_2+l_3+l_4}^{l_1+l_2+l_3+l_4+l_5} p_5\left(x\right)x\,dx=0 \tag{7}$$

$$\sum F_y=0$$
$$V_w-\int_0^{l_1} p_1\left(x\right)dx+\int_{l_1}^{l_1+l_2} w_2\left(x\right)S\;dx-\int_{l_1+l_2}^{l_1+l_2+l_3} p_3\left(x\right)\;dx$$
$$+\int_{l_1+l_2+l_3}^{l_1+l_2+l_3+l_4} w_4\left(x\right)S\;dx-\int_{l_1+l_2+l_3+l_4}^{l_1+l_2+l_3+l_4+l_5} p_5\left(x\right)\;dx=0 \tag{8}$$

In **Eq. (7)** and **Eq. (8)**, the bending moment and shear force at $x = l_1$, $x = l_1 + l_2$, $x = l_1 + l_2 + l_3$ and $x = l_1 + l_2 + l_3 + l_4$ are functions of unknown coefficients in the free body diagram developed for the region of interest along the shingle. For example, for a free body diagram of Region 1 ($0 \le x \le l_1$ in Figure 2.1b), $M(x = l_1)$ is a function of M_w, V_w, and C_1 through C_4. The constants of integration C_1 through C_{20} are obtained using 20 equations that are representative of the boundary conditions defined in Table 2.2.

This set of equations can be solved as a system of linear equations by means of **Eq. (9)**:

$$\left[B\right]\left\{C\right\}=\left\{b\right\} \tag{9}$$

as demonstrated by Croom et al. (2015a) for the case of shingle tabs with one sealant strip. In **Eq. (9)**: the rows in matrix [B] include the coefficients obtained from the integration and differentiation of **Eq. (2)** through **Eq. (6)** for specific beam coordinates (x in Figure 2.1),

and accounting for the boundary conditions presented in Table 2.2; vector $\{C\}$ includes the constants of integration (C_1 through C_{20}); and vector $\{b\}$ includes factors obtained from the integration of applicable loading and geometry parameters.

2.2 SHINGLE-SEALANT BOND ENERGY RELEASE RATE

The energy release rate, G, can be used as a measure of shingle-sealant bond strength, and the uplift displacement of the shingle can be calculated at any location ($0 \leq x \leq l_1 + l_2 + l_3 + l_4 + l_5$ in Figure 2.1b) based on the methodology described in **Eq. (1)** through **Eq. (8)**. Therefore, simulations provide a direct means to determine the applied G values along the inner and outer edge of both sealant strips. The uplift force per unit area at an arbitrary position x along the two sealant strips (*i.e.*, Region 2 in the domain $l_1 \leq x \leq l_1 + l_2$ for the inner strip, and Region 4 in the domain $l_1 + l_2 + l_3 \leq x \leq l_1 + l_2 + l_3 + l_4$ for the outer strip, in Figure 2.1b) is given as $S\,w_i(x)$, where $w_i(x)$ is the uplift displacement of the sealant material, with $i = 2$ and $i = 4$ corresponding to the inner and outer sealant strips, respectively. Thus, G can be determined at an arbitrary position x for either sealant strip (along Region 2 and Region 4 in Figure 2.1b) using the following expression:

$$G(x) = \int S w_i(x)\, dw_i = \frac{1}{2} S \left[w_i(x) \right]^2 \quad \text{for } i = 2, 4 \tag{10}$$

In this study, the applied G values at the inner and outer edges of both sealant strips are used to identify potential initiation sites for peeling-type failure of asphalt roof shingles. Such failures are representative of real-case scenarios (Shiao et al. 2003b, Ghorbani et al. 2015).

Table 2.1 Asphalt roof shingle-sealant structural model parameters and dimensional units.

Notation	**Parameter**	**Dimensional unit**[1]
l	Length of shingle (along axis x)	L
l_1	Distance between nail line and inner edge of inner sealant strip (along axis x)	L
l_2	Length of inner sealant strip (along axis x)	L
l_3	Distance between outer edge of inner sealant strip and inner edge of outer sealant strip (along axis x)	L
l_4	Length of outer sealant strip (along axis x)	L
l_5	Length of leading edge of shingle (along axis x)	L
W	Width of shingle element (along axis z)	L
E	Elastic modulus of shingle material (along axis x)	FL^{-2}
S	Stiffness of elastic foundation (sealant strip) per unit thickness (along axis y)	FL^{-3}
I	Shingle cross-sectional area moment of inertia (with respect to axis z)	L^4
EI	Flexural stiffness of shingle cross section (with respect to axis z)	FL^2
p_1	Out-of-plane surface pressure on shingle surface between nail line and inner edge of inner sealant strip	FL^{-2}
p_3	Out-of-plane surface pressure on shingle surface between outer edge of inner sealant strip and inner edge of outer sealant strip	FL^{-2}
p_5	Out-of-plane surface pressure on shingle leading edge	FL^{-2}
G	Applied energy release rate at sealant strip edge	FL^{-1}

[1] F = force; L = length.

Table 2.2 Model boundary conditions and continuity equations

Parameter	$x = 0$	$x = l_1$	$x = l_1 + l_2$	$x = l_1 + l_2 + l_3$	$x = l_1 + l_2 + l_3 + l_4$
Out-of-plane deflection	$w_1 = 0$	$w_1 = w_2$	$w_2 = w_3$	$w_3 = w_4$	$w_4 = w_5$
Slope of deflected shape	$w_1' = 0$	$w_1' = w_2'$	$w_2' = w_3'$	$w_3' = w_4'$	$w_4' = w_5'$
Bending moment	$EIw_1'' = M_w$	$EIw_1'' = EIw_2''$	$EIw_2'' = EIw_3''$	$EIw_3'' = EIw_4''$	$EIw_4'' = EIw_5''$
Shear force	$EIw_1''' = -V_w$	$EIw_1''' = EIw_2'''$	$EIw_2''' = EIw_3'''$	$EIw_3''' = EIw_4'''$	$EIw_4''' = EIw_5'''$

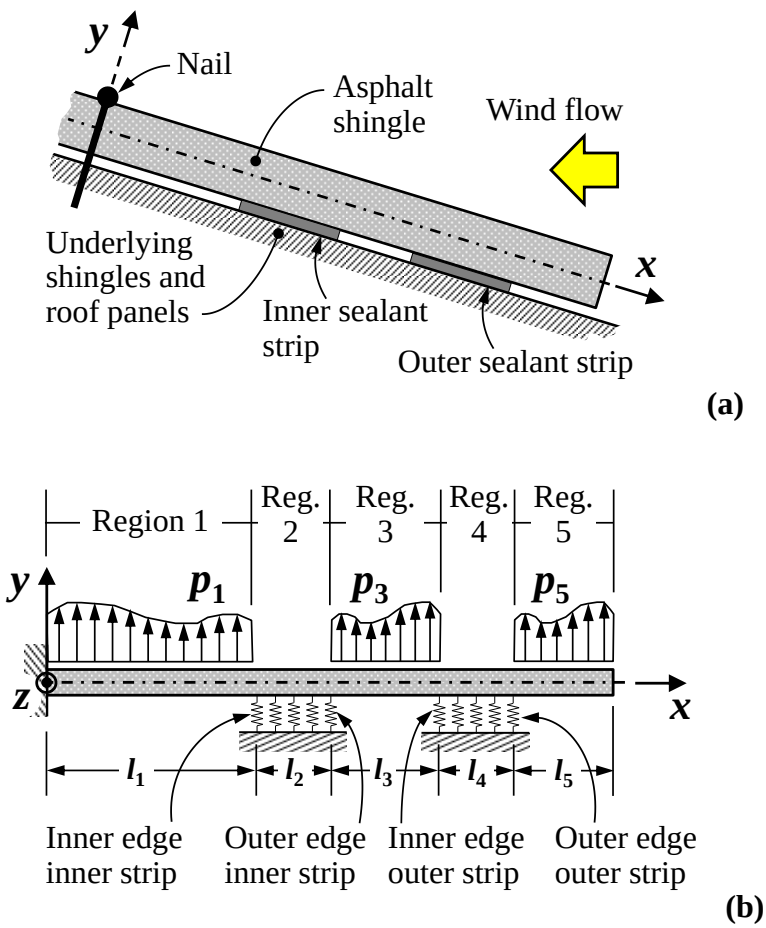

Figure 2.1 Structural model: (a) schematic of asphalt roof shingle-sealant system; and (b) loading and boundary conditions. Note that axis *z* is perpendicular to axis *x* and *y*.

CHAPTER 3

PARAMETRIC STUDY OF SHINGLE-SEALANT STRUCTURAL RESPONSE

The analytical model presented herein was used to predict the uplift response of a roof asphalt shingle having two sealant strips. Then, the applied energy release rate, G, at the inner and outer edges of both sealant strips (Region 2 and Region 4 in Figure 2.1b) was calculated using **Eq. (10)**.

The nominal dimensions used in the representative shingle-sealant structural model include (Table 2.2 and Figure 2.1b): sealant strip thickness, t = 0.0028 m; shingle flexural stiffness, EI = 0.234 N-m^2; sealant elastic stiffness, S = 4.53 GPa/m; sealant strip length, $l_2 = l_4$ = 0.0127 m (mimicking typical values in commercially available self-sealing strips); shingle length, $l_1 + l_2 + l_3 + l_4 + l_5$ = 0.1334 m; and, distance between the nail line and the inner edge of the outer strip, $l_1 + l_2 + l_3$ = 0.105 m (*i.e.*, assuming a length for the leading edge portion, Region 5 in Figure 2.1b, l_5 = 0.0154 m as often found in commercially available three-tab asphalt roof shingles). Assuming a nominally elastic response of both the sealant and shingle substrate, two material properties are required to model the shingle-sealant uplift response: the modulus of elasticity of the shingle material in the x-direction, E; and, the elastic stiffness of the sealant per unit thickness, S, in the y-direction (Table 2.1, Figure 2). In the parametric study presented in this section, these parameters are E = 280 MPa and S = 4.53 GPa/m as derived through physical experiments on representative shingle and sealant materials reported by Croom et al. (2015a).

The mechanical model originally formulated and validated by Peterka et al. (1997, 1999) was used to estimate the uplift pressures along the shingle length. The introduction of an additional sealing strip was accounted for by assuming a similar uplift pressure in Region 1 and Region 3 (*i.e.*, $p_1 = p_3$), as shown in Figure 3.1. For a wind height of 9.24 m and mean roof height of 4.62 m, assuming a 3-s peak gust of 241 km/h associated with a "H-rating" for asphalt roof shingles (ASTM 2011), the resulting constant uplift pressures are $p_1 = p_3 = 507$ Pa, and $p_5 = 2028$ Pa. These pressure values were input in the analytical model to perform a parametric study for the following significant variables and ranges:

- Distance between outer edge of inner sealant strip and inner edge of outer sealant strip (*i.e.*, clear spacing between the inner and outer strip shown as Region 3 in Figure 3.1), $0 \leq l_3 \leq (0.1334 - l_2 - l_4 - l_5)$ where the upper bound in associated with $l_1 = 0$.
- Distance between outer edge of outer sealant strip and leading edge of the shingle (*i.e.*, length of shingle lip shown as Region 5 in Figure 3.1), $0 \leq l_5 \leq 0.0154$ m.
- Elastic stiffness of sealant strip, $1 \leq S \leq 10$ GPa/m to reflect the potential for physical changes due to temperature effects and aging (Shiao et al. 2003a, Berdahl et al. 2008, Dixon et al. 2014a, 2014b).

The forward method for the analytical shingle-sealant structural model was implemented in Python v3.3 using the numerical package NumPy (Oliphant 2006), performing all calculations with double-floating point precision.

3.1 ASSUMPTIONS AND LIMITATIONS OF MECHANICAL MODEL

The salient assumptions and limitations of the proposed mechanical model were identified in a previous study for the case of shingles with one sealant strip (Croom et al.

2015a, 2015b), and are summarized as follows.

- Shingle uplift is constant along the entire width of a given shingle tab, *i.e.*, $w_i(x)$ does not change along the width direction, z.
- Shingle and sealant materials deform elastically.
- Sealant strip is continuous across its width, *i.e.*, effects associated with possible premature local delamination along intermittent sealant strips (*e.g.*, Figure 1.1) are neglected.

In this study, another potential limitation is represented by the assumption that $p_1 = p_3$ for a two-sealant strip configuration, though to the best of the authors' knowledge no experimental evidence is available regarding actual pressures.

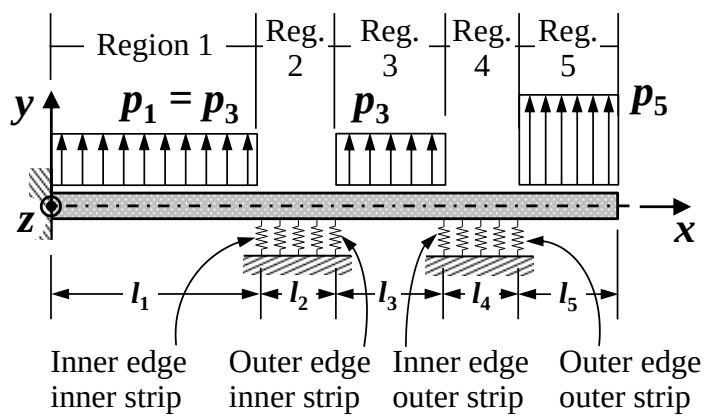

Figure 3.1 Structural model used in parametric study, with $p_1 = p_3 = 507$ Pa and $p_5 = 2028$ Pa, after Peterka et al. (1997).

CHAPTER 4

RESULTS AND DISCUSSIONS OF PARAMETRIC STUDIES

Simulation results are presented to: (a) discuss the sensitivity of the applied energy release rate, G, at the inner and outer sealant edges of both adhesive strips with respect to shingle geometry (*i.e.*, position of constant-length sealant strips, and shingle lip length) and elastic stiffness of the sealant strip material; (b) determine the most suitable position for the two sealant strips along the length of the shingle tab by minimizing the maximum applied G; and (c) compare this shingle configuration with conventional counterparts having one sealant strip based on their maximum G, and understand to what extent adding a second sealant strip is convenient from a mechanical standpoint.

4.1 INFLUENCE OF SEALANT STRIP LOCATION ON APPLIED *G* AT SEALANT STRIP EDGES

In Figure 4.1, the applied G at the inner and outer edge of both sealant strips is presented as a function of the clear spacing between the sealant strips, assuming a constant length for the shingle tab ($l_1 + l_2 + l_3 + l_4 + l_5 = 0.1334$ m), sealant strips ($l_2 = l_4 = 0.0127$ m), and shingle lip ($l_5 = 0.00154$ m), *i.e.*, for $0.0926 \text{ m} \leq l_3 \leq 0 \text{ m}$ or $0 \leq l_1 \leq 0.0926$ m. The applied G at the inner edge of the inner sealant strip ($x = l_1$) increases nonlinearly with increasing values of l_1 (*i.e.*, as the inner sealant strip is positioned away from the shingle nail line, $x = 0$, and l_3 is reduced) as illustrated in Figure 4.1a. This trend is reversed for the outer edge of the inner sealant strip ($x = l_1 + l_2$) as the applied G rapidly decreases with increasing values of l_1, and is similar to the trend of the applied G at the inner edge of the

outer sealant strip ($x = l_1 + l_3$) as shown in Figure 4.1b, reflecting the fact that both edges are subject to an approximately symmetric loading condition as produced by the uplift pressure p_3 along l_3, irrespective of the l_1 value (Figure 3.1). Instead, for the constant shingle lip length l_5 = 0.00154 m, the position of the inner sealant strip has minor effects on the applied G at the outer edge of the outer sealant strip, which lies within the range 0.27-0.28 J/m^2 (Figure 4.1b), reflecting the fact that this edge is directly exposed to wind loads (Figure 2.1a). Otherwise, the maximum applied G is minimized for l_1 = 0.049 m (G = 0.025 J/m^2).

Theoretically, it is possible to minimize the maximum applied G at this sensitive location (outer edge of the outer sealant strip) by using zero-lip shingle tabs. This is illustrated in Figure 4.2 where the applied G at the inner and outer edge of both sealant strips is presented as a function of the clear spacing between the sealant strips, assuming a constant length for the shingle tab ($l_1 + l_2 + l_3 + l_4 + l_5$ = 0.1334 m) and sealant strips ($l_2 = l_4$ = 0.0127 m), and a zero-length shingle lip (l_5 = 0 m), *i.e.*, for 0.108 m $\leq l_3 \leq$ 0 m or 0 $\leq l_1 \leq$ 0.108 m. As expected, the trend for the applied G at the inner and outer edge of the inner sealant strip (Figure 4.2a) mimics that for the case of l_5 = 0.00154 m (Figure 4.1a). Here, higher peak values of applied G are attained due to the larger maximum length of either Region 3 (l_3) or Region 1 (l_1) subject to the uplift pressure $p_1 = p_3$ = 507 Pa. The same applies to the applied G at the inner edge of the outer sealant strip (Figure 4.2b) compared to the case where l_5 = 0.00154 m (Figure 4.1b) whereas $G \approx 0$ J/m^2 at the outer edge since l_5 = 0 m. If this configuration was considered while disregarding the practical difficulty of manufacturing and effectively installing shingles with zero-length lips, then failure due to delamination would be governed by the applied G at all other sealant strip

edges. In fact, G_{min}, defined as the greatest lower bound of G for all four sealant strip edges, would be minimized for l_1 = 0.056 m (G_{min} = 0.046 J/m^2).

The parametric analysis presented above and summarized in Figure 4.1 and Figure 4.2 shows that when two sealant strips are used, as the inner sealant strip is moved away from the nail line and toward the outer sealant strip (by increasing l_1), the applied G: increases at the inner edge of the inner sealant strip; decreases with a similar gradient at the outer edge of the inner sealant strip and at the inner edge of the outer sealant strip; and remains nearly constant at the outer edge of the outer sealant strip. Therefore, for a nominal sealant strip length (l_2 = l_4 = 0.0127 m in Figure 3.1), there exists a shingle-sealant configuration (*i.e.*, position for the two sealant strips given by $x = l_1$ and $x = l_1 + l_2 + l_3$, respectively) where the maximum energy release rate at any of the sealant strip edges is minimized.

Based on the simulation results, for a set of given shingle lip length values (l_5), Table 4.1 summarizes the G_{min} values and the associated position of the inner sealant strip (l_1). It is noted that the optimal G_{min} (*i.e.*, lower-bound G for all sealant strip edges) is attained for a shingle configuration where l_5 = 0.008 m. This is illustrated in Figure 4.3 where the applied G at the inner and outer edge of both sealant strips is presented as a function of the clear spacing between the sealant strips, assuming a constant length for the shingle tab ($l_1 + l_2 + l_3 + l_4 + l_5$ = 0.1334 m), sealant strips ($l_2 = l_4$ = 0.0127 m), and shingle lip (l_5 = 0.008 m), *i.e.*, for 0.1 m $\leq l_3 \leq$ 0 m or $0 \leq l_1 \leq$ 0.1 m. For l_1 = 0.052 m and l_3 = 0.0479 m, the applied G is similar for all edges of both sealant strips, resulting in a minimized G_{min} = 0.034 J/m^2 (Figure 4.3 and Table 4.1).

4.2 COMPARISON WITH STANDARD ASPHALT-SHINGLE SYSTEM WITH ONE SEALANT STRIP

Based on simulations of conventional asphalt roof shingles with one sealant strip, the optimal value of G_{min} under 241-km/h 3-s gusts is approximately 0.48 J/m^2 (Croom et al. 2015a, 2015b). This applied energy release rate value lies in the upper bound of the range 0.10-0.51 J/m^2 for peeling-type failures, which was estimated (Croom et al. 2015a) based on "T-pull" test data reported by Shiao et al. (2003b) for one-layer asphalt roof shingles. Therefore, it is important to note that the introduction of a second sealant strip at l_1 = 0.0521 m (Figure 3.1), in conjunction with the use of a lip length l_5 = 0.008 m, and sealant strip length $l_2 = l_4$ = 0.0127 m, transforms the uplift resistance of the shingle-sealant system subject to 241-km/h 3-s gusts (*i.e.*, "H-rated" per ASTM 2011). In fact, the resulting G_{min} = 0.034 J/m^2 (Figure 4.3 and Table 4.1) for a standard 0.1334-m long shingle tab is almost 14 times smaller than that that of one-sealant strip counterparts.

It is noted that G_{min} for optimized configurations lies in the range 0.034-0.046 J/m^2 for $0 \leq l_5 \leq 0.008$ m, as illustrated in Figure 4.4. However, it becomes more sensitive to increases in the shingle lip length past l_5 = 0.008 m (*i.e.*, as the outer sealant strip is shifted toward the nail line), reaching values that are one order of magnitude higher, up to 0.14 J/m^2 for l_5 = 0.0127 m, and 0.27 J/m^2 for l_5 = 0.0154 m. The latter value is still nearly half of that for optimized one-sealant strip systems. Nonetheless, from a practical standpoint, it is important to position the outer sealant strip closer to the leading edge compared to optimized one-sealant strip configurations to take full advantage of a two-sealant strip configuration.

4.3 INFLUENCE OF SEALANT STIFFNESS ON APPLIED *G* AT SEALANT STRIP EDGES

The material properties of modern asphalt roof shingle-sealant systems are susceptible to changes due to environmental exposure (*e.g.*, temperature) (Shiao et al. 2003a, Berdahl et al. 2008, Dixon et al. 2014a, 2014b). Therefore, it is of interest to assess the influence of stiffness changes in the sealant strip on the applied energy release rate, G, when using two-sealant strip configurations. To this end, based on the mechanical model shown in Figure 3.1, simulations were performed to estimate G_{min} for selected values of S in the range 1-10 GPa/m, assuming a shingle lip length l_5 = 0.008 m, and uplift pressures $p_1 = p_3$ = 507 Pa and p_5 = 2028 Pa from 241-km/h 3-s gusts. While S = 4.53 GPa/m was estimated as a representative value for commercially available sealant materials based on physical tests (Croom et al. 2015a), analyzing results for the range 1-10 GPa/m is intended to account for realistic scenarios of either softening or embrittlement of the sealant material.

The simulation results for S = 1, 2, 4.53, 7 and 10 GPa/m are presented in Table 4.2, including G_{min} values and the position of this sealant strip (l_1). These results indicate that G_{min} and the optimal positioning of both sealant strips are weak functions of the sealant stiffness for $1 \leq S \leq 10$ GPa/m. These results are important since they confirm that, by selecting the position of both sealant strips based on the minimization of G_{min}, significant softening or embrittlement of the sealant material produces negligible changes in G_{min}, which remains in the range 0.029-0.040 J/m^2 (Table 4.1).

Table 4.1 Simulation results for G_{min} and corresponding l_1 (distance between nail line and inner edge of inner sealant strip) for fixed l_5 (shingle lip length)

l_5 [m]	G_{min} [J/m^2]	l_1 [m]
0	0.0460	0.0562
0.0035	0.0408	0.0544
0.0063	0.0360	0.0528
0.0080	0.0341	0.0521
0.0095	0.0580	0.0596
0.0127	0.1450	0.0719
0.0154[2]	0.2741	0.0690

Table 4.2 – Simulation results for G_{min} and corresponding l_1 (distance between nail line and inner edge of inner sealant strip) for fixed S (sealant elastic stiffness parameter)

S [GPa/m]	G_{min} [J/m^2]	l_1 [m]
1.00	0.0295	0.0504
2.00	0.0325	0.0508
4.53[3]	0.0341	0.0521
7.00	0.0353	0.0517
10.0	0.0397	0.0534

[2] Representative lip length for commercially available asphalt roof shingles.
[3] Representative sealant stiffness per unit thickness for commercially available asphalt roof shingles.

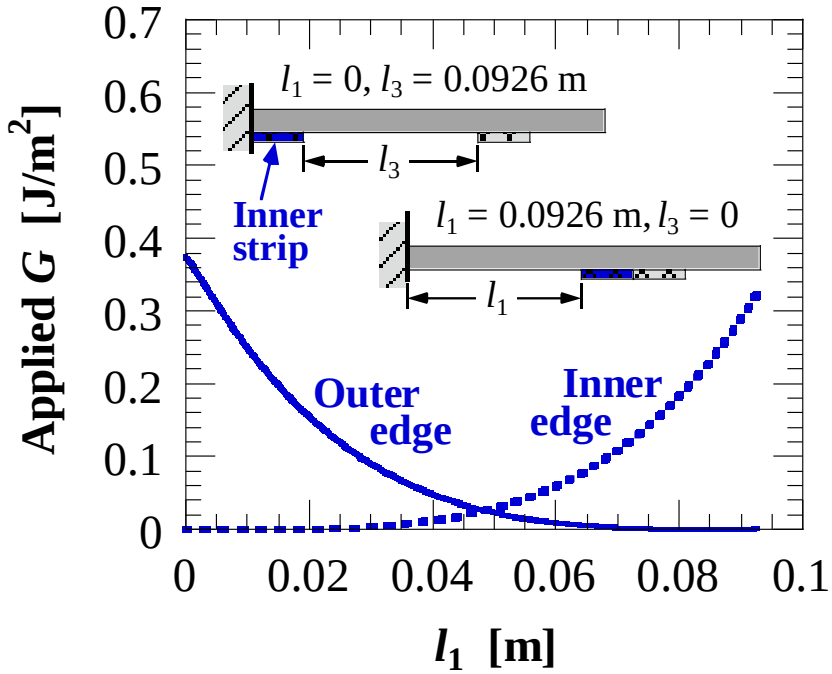

(a)

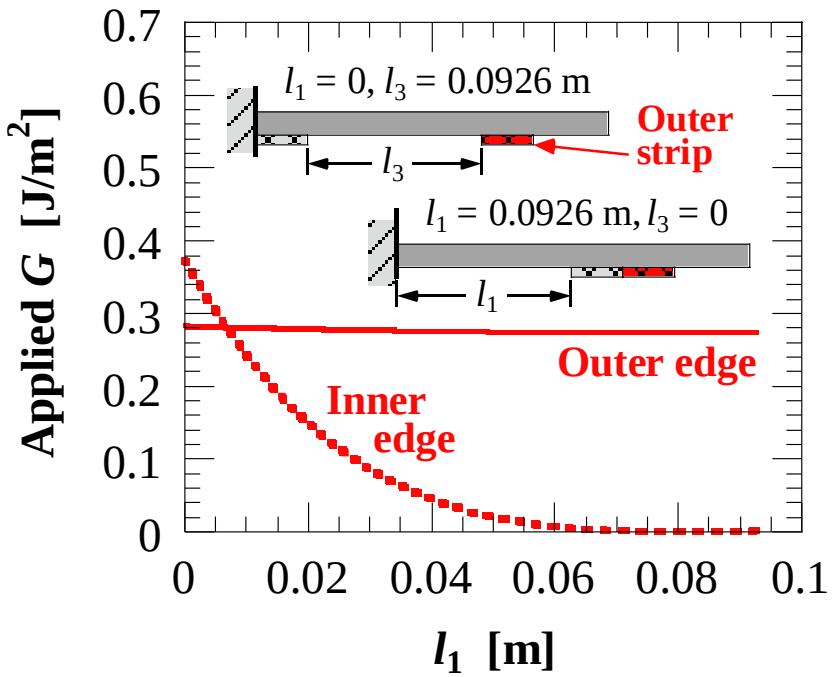

(b)

Figure 4.1 Applied G at sealant strip edges as function of clear spacing between sealant strips (l_3 in Figure 3.1), *i.e.*, by varying l_1 for constant sealant strip length ($l_2 = l_4 = 0.0127$ m), shingle lip length ($l_5 = 0.00154$ m), and total shingle tab length ($l_1 + l_2 + l_3 + l_4 + l_5 = 0.1334$ m): (a) inner and outer edge of inner sealant strip; and (b) inner and outer edge

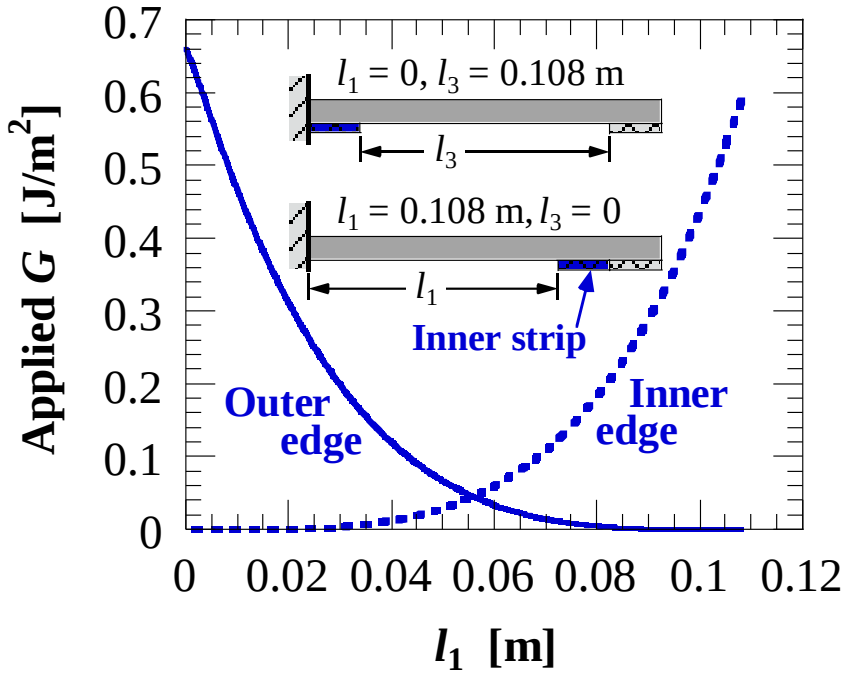

(a)

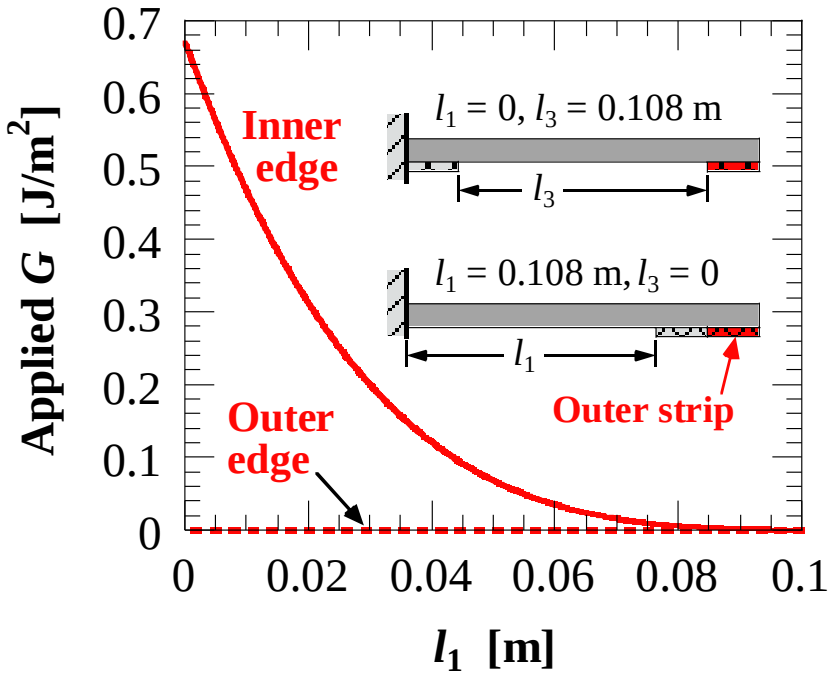

(b)

Figure 4.2 Applied G at sealant strip edges as function of clear spacing between sealant strips (l_3 in Figure 3.1), *i.e.*, by varying l_1 for constant sealant strip length ($l_2 = l_4 = 0.0127$ m), shingle lip length ($l_5 = 0$ m), and total shingle tab length ($l_1 + l_2 + l_3 + l_4 + l_5 = 0.1334$ m): (a) inner and outer edge of inner sealant strip; and (b) inner and outer edge of

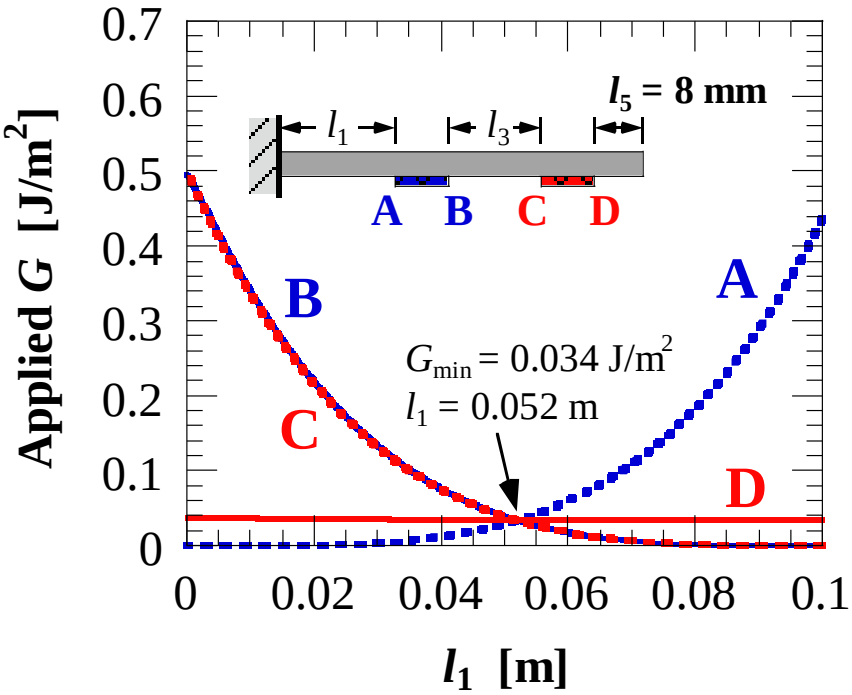

Figure 4.3 Applied G at sealant strip edges as function of clear spacing between sealant strips (l_3 in Figure 3.1), *i.e.*, by varying l_1 for constant sealant strip length ($l_2 = l_4 = 0.0127$ m), shingle lip length ($l_5 = 0.008$ m), and total shingle tab length ($l_1 + l_2 + l_3 + l_4 + l_5 = 0.1334$ m). Note minimized $G_{min} = 0.034$ J/m^2 for $l_1 = 0.052$ m.

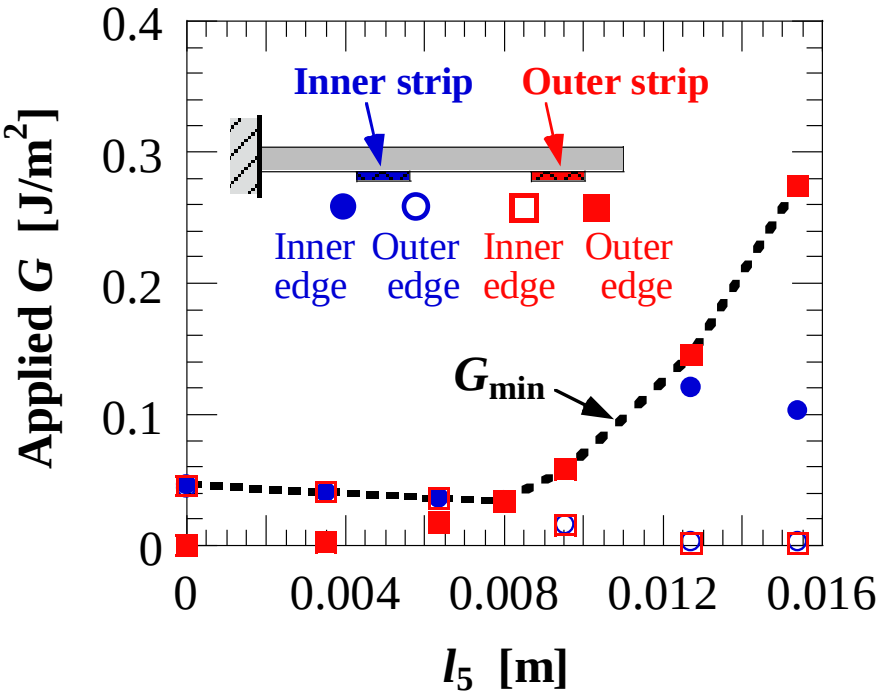

Figure 4.4 Applied G at all sealant strip edges for selected shingle lip length (l_5) values, and associated G_{min} for optimal configuration (consistent with simulation results and l_1 values in Table 4.1).

CHAPTER 5

CONCLUSIONS TO MODELING OF DOUBLE SEALANT SYSTEMS

A beam-on-elastic-foundation (BOEF) model was formulated and used to simulate the structural response of one-layer asphalt roof shingles with two sealant strips, subject to uplift pressures representative of 241-km/h 3-s gusts. The following conclusions are drawn.

1) For a given shingle tab length and sealant strip length, data mining of the simulation results demonstrates that there exists an optimal geometric configuration that minimizes the applied energy release rate associated with peeling-type failure at the sealant strip edges.
2) The minimized applied energy release rate is strongly dependent on the position of the sealant strips. To radically enhance uplift resistance (and, in turn, longevity), it is shown that modern one-layer asphalt roof shingle systems with one sealant strip can be modified by: (a) shifting the existing sealant strip closer to the free edge to reduce the applied G at the outer edge near the leading edge of the shingle; and (b) adding a second sealant strip approximately half way between the outer sealant strip and the nail line, thereby ensuring that similar applied G values are attained at both edges of the inner sealant strip and the inner edge of the outer sealant strip.
3) Uplift resistance is insensitive to changes by one order of magnitude in the elastic stiffness of the sealant material ($1 \leq S \leq 10$ GPa/m). Thus, significant softening or embrittlement of the sealant material will have negligible effects on the applied G

values.

4) Though the applied *G* values are not appreciably affected by changes in the elastic stiffness of the sealant material, long-term exposure to the environment may reduce the strength of the shingle-sealant bond (which can be quantified by a reduction in the critical applied energy release rate). If environmental degradation is of concern, an additional advantage of incorporating a second sealant strip is that it will take a longer exposure time and continuing reductions in the critical applied energy release rate before bond failure takes place, thereby increasing the design life of the shingle.

CHAPTER 6

INTRODUCTION TO SEALANT CHARACTERIZATION AND MODELING OF SEALANT EXHIBITING VISCOELASTIC RESPONSE

Conventional asphalt shingles typically utilize self-sealing adhesive strips which bond the lower roof shingle to the one placed on top of it (Figure 1.1), with modern asphalt roof-sealant structures utilizing a single self-sealing strip. Croom et al. (2015a, 2015b) developed and used a beam-on-elastic-foundation (BOEF) model, with both the foundation and the shingle body assumed to respond elastically throughout the loading, to simulate the uplift response of such a structure undergoing 150-mph winds. Based on the results of the numerical simulations, Croom et al. (2015a) determined the optimal position for a single self-sealing adhesive strip. In the first several chapters of this thesis, a modified version of the Croom et al. (2015a) BOEF model was developed in order to simulate the uplift response of a double sealant-strip roof-shingle system undergoing 150-mph 3-s gusts and locate the optimal locations of the two sealants when undergoing elastic deformations.

Since the sealant strip material is a form of bitumen, it falls into the category of viscoelastic materials (Shiao et al. 2003a, National Roofing Contractors Association 2003), where a material is characterized as a function of time. (Emri et al. 2010). In Chapter 7, a brief description of the theory for a viscoelastic material system is presented. In Chapter 8, the experimental studies performed in this study to obtain specific viscoelastic properties through the use of a Dynamic Mechanical Analyzer are described and results presented. In Chapter 9, details regarding the simulations of sealant viscoelastic response

are presented, along with results for one and two sealant strip roof-shingle systems placed in optimal positions and undergoing loading consistent with 150-mph 3-s gusts that continue for 1 hour and 5 hours. The simulations are performed in ANSYS Mechanical APDL by incorporating the viscoelastic properties of the sealant material into the numerical models. Chapters 10 and 11 present a Discussion and Conclusions, respectively, for the viscoelastic studies. Chapter 12 presents limitations of current studies and future work.

CHAPTER 7

THEORETICAL BACKGROUND

7.1 DERIVATION OF VISCOELASTIC CREEP LAW

The viscoelastic behavior of the shingle sealant material used in modern shingle-sealant roof systems is modeled as a Standard Linear Solid; a schematic of this model is shown in Figure 7.1. The Standard Linear Solid model is capable of instantaneous elongation and, as such, is comprised of a linear viscous damper in series with a Kelvin-Voigt solid (Wineman et al. 2000). The model is comprised of a linear damper with a modulus of elasticity of E_1, a linear damper in the Kelvin-Voigt solid with a modulus of elasticity of E_2, and a dashpot with an apparent extensional viscous coefficient of η_e (Kelly 2015). The standalone linear damper is simulated in ANSYS by using a LINK180 element to simulate the linear viscous damper that is in series with the Kelvin-Voigt solid. The Kelvin-Voigt solid is simulated through the use of a built-in ANSYS Generalized Exponential Implicit Creep Law (GEICL) with coefficients chosen to make the creep law behave like the creep law of a Standard Linear Solid.

To use the GEICL within ANSYS, a set of derivations is required. Starting with the definition of extensional viscosity, η_e, as (Franck 2011);

$$\eta_e(t) = \frac{\sigma_t(t)}{\dot{\varepsilon}_t(t)} \tag{1}$$

the governing equation of the Standard Linear Solid formulation is given by **Eq. (2)** (Kelly 2015). By assuming a constant stress, σ_0, the formulation in **Eq. (2)** can be simplified into

Eq. (3) and the strain $\varepsilon(t)$ can be expressed by the formulation in **Eq. (4)** (Kelly 2015). By substituting **Eq. (4)** into **Eq. (3)**, we obtain **Eq. (5)**, a creep law for the Standard Linear Solid. The derived creep law compatible with the ANSYS GEICL formulation is given in **Eq. (6)** under the assumption of constant stress. The five constants in **Eq. (6)** are obtained by matching **Eq. (5)** with **Eq. (6)** and are determined to have the following values: $C_1 = 1/E_2\,, C_2 = 1, C_3 = 0, C_4 = 0\ and\ C_5 = E_2/\eta_e$.

$$\sigma(t) + \frac{\eta_e}{E_1 + E_2}\dot{\sigma}(t) = \frac{E_1 E_2}{E_1 + E_2}\varepsilon(t) + \frac{E_1 \eta_e}{E_1 + E_2}\dot{\varepsilon}(t) \tag{2}$$

$$\dot{\varepsilon}(t) = \frac{E_1 + E_2}{E_1 \eta_e}\left[\sigma_0 - \frac{E_1 E_2}{E_1 + E_2}\varepsilon(t)\right] \tag{3}$$

$$\varepsilon(t) = \sigma_0\left[\frac{1}{E_1}e^{-(E_2/\eta_e)t} + \frac{E_1 + E_2}{E_1 E_2}\left(1 - e^{-(E_2/\eta_e)t}\right)\right] \tag{4}$$

$$\dot{\varepsilon}(t) = \frac{\sigma_0}{\eta_e}e^{-(E_2/\eta_e)t} \tag{5}$$

$$\dot{\varepsilon}(t) = C_1\sigma(t)^{C_2} r e^{-rt}, r = C_5\sigma(t)^{C_3} e^{-C_4 t} \tag{6}$$

7.2 DERIVATION OF VISCOELASTIC CONSTANTS

The formulations for the model parameters E_1 and E_2 are determined through the use of three assumptions: constant stress (**Eq**. **(3)**; at a small time t_0 the dashpot in the Kelvin-Voigt unit is fully collapsed ($\eta_e = 0$ in **Eq. (4)**); at very large time, t_∞, the dashpot is fully extended ($\eta_e = \infty$ in **Eq. (4)**). By using the first assumption, it is found that the contribution to stress in the model comes from only the linear damper with a modulus of elasticity E_1. Since there is no contribution from the dashpot and no strain rate coefficient, E_1 must therefore be equal to the elastic modulus of the material. Similarly, from the second assumption, the contribution to the stress in the model comes from both the spring with

elastic modulus E_1 as well as the spring with elastic modulus E_2 for a total modulus of E_∞, known as the relaxation modulus. The relaxation modulus is calculated from a creep experiment through the expression in **Eq. (7)** (Gerdeen et al. 2006). From **Eq. (4)**, when t →∞, the relationship between the constant applied stress and the final strain can be written in the form

$$E_\infty = \frac{\sigma_0}{\varepsilon_\infty} \tag{7}$$

The coefficient, E_2 is obtained by applying the rule for springs in series, as shown in **Eq. (8)**.

$$E_2 = (E_\infty^{-1} - E_1^{-1})^{-1} \tag{8}$$

The time dependent effective extensional viscous coefficient, $\eta_e(t)$, is calculated through the relationship shown in **Eq. (4)**, where $\sigma_t(t)$ and $\dot{\varepsilon}_t(t)$ are true stress and true strain rate, respectively (Franck 2011). Since a Standard Linear Solid formulation generally employs constant values for η_e, in this study the value of viscosity corresponding to the final simulation time is used. Thus, the value of η_e is obtained from **Eq. (1)** when evaluated at t_{final}.

7.3 SHINGLE-SEALANT FAILURE MODELS AND BOND ENERGY RELEASE RATE

In the first part of this thesis, energy release rate, *G*, was used to predict the onset of sealant separation under nominally elastic conditions. For materials undergoing nominally creep conditions, parameters such as the strain at fracture (Chambers 2000) can serve as a measure of shingle-sealant bond strength. Another parameter that has been suggested for use in predicting the onset of creep fracture is energy release rate [Cheng

(2013), Surimamilla (2013) and Życzkowski (1991)]. As noted by Knauss (Knauss, 1989) once a flaw has formed then G through the J-integral formulation is also a potentially viable fracture parameter for viscoelastic materials. Both parameters can be calculated using output from the FEA models described above. Specifically, the models have the ability to output the stress and strain of an asphalt shingle at any location and at any time *t*. To compute G at any time, **Eq. (9),** where x is location along a sealant strip and σ_t is the true stress, can be used in conjunction with thickness of the sealant, a, to determine values of *G*.

$$G(x,t) = a \cdot \int_0^{\varepsilon_t} \sigma_t(x,t)\, d\varepsilon \tag{9}$$

This study focuses on the values of *G* at the inner and outer edges of the sealant of the single sealant system, as well as the inner and outer edges of the inner and outer sealants in the double sealant shingle configuration.

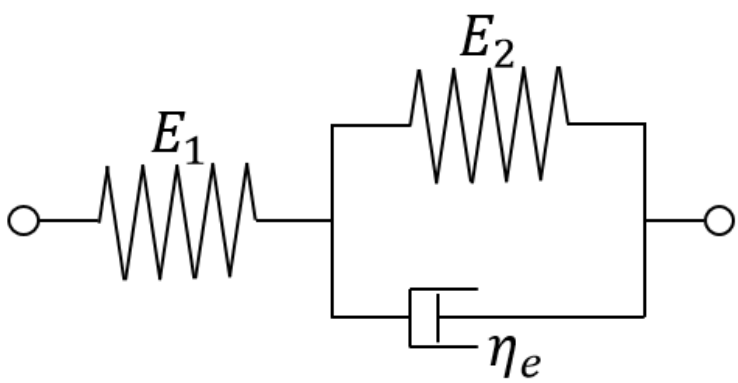

Figure 7.1 Standard Linear Solid model comprised of a linear damper with modulus E_1 in series with a Kelvin-Voigt unit comprised of a linear damper with modulus E_2 and a dashpot with an effective extensional viscosity of η_e.

CHAPTER 8

CHARACTERIZATION OF SEALANT MATERIAL

Two types of experiments were conducted on the sealant material in order to determine the material properties necessary for viscoelastic modeling: (1) uniaxial compression experiment for the determination of the Young's Modulus, E_1, and (2) uniaxial compression creep experiments for the determination of the critical viscoelastic energy release rate, G_c, the Relaxation Modulus, E_∞, the Young's Modulus of the linear damper in the Kelvin-Voigt unit, E_2, and the effective extensional viscosity, η_e. All of the experiments use the RSA III Dynamic Mechanical Analyzer and specimens of cylindrical shape.

8.1 MANUFACTURING OF SPECIMENS

Owens Corning Supreme shingles purchased in Columbia, SC in early 2016 serve as the source of sealant material for the experiments. For our experiments, the thermoplastic sealant material is removed carefully from the shingles using either a razor blade or a similar sharp tool and inspected to ensure that no foreign matter is present. To convert the small pieces of sealant into a usable specimen, a cylindrical steel mold was designed and manufactured. The steel mold and a typical sealant specimen are shown in Figure 8.1 and Figure 8.2, respectively. To convert the fragments into cylindrical specimens, prior to heating the mold for specimen fabrication the inside of the mold is coated with Frekote 770-NC mold release. After coating the internal surfaces, the base of the mold is subsequently heated to 150 degrees Celsius (ºC) on a hot plate. The collected

sealant material is then incrementally added to the mold until the mold is full of molten sealant material. After turning the hot plate off, the material is left to cool for approximately an hour inside of the mold. Once the mold has cooled to near room temperature, the specimen is removed from the mold. Each specimen is ~13.5 mm long and ~ 15 mm in diameter; the length is the maximum that can be tested using existing DMA fixtures. The dimensions of Specimens 1 through 6, the specimens manufactured and used for experimentation appear in Table 8.1. Once an experiment has been conducted, the old specimen is recovered. The specimen is then broken down and reformed into a new specimen through the process described above for further creep experiments at different temperatures.

8.2 UNIAXIAL COMPRESSION TEST AND THE YOUNG'S MODLUS OF THE SEALANT MATERIAL

To measure Young's Modulus of the sealant material, E_1, specimen 1 was loaded in nominally uniaxial compression between two lubricated platens (oil was used for lubrication) by the RSA III test system. A photograph of a specimen inside the RSA III test system between two platens is shown in Figure 8.3. Loading was applied at a quasi-static loading rate of 2.571×10^{-4} m/m per second until a compressive strain of 8.6% was attained. As the specimen was compressed, its diameter grew radially outward towards the outer edge of the grip (Figure 8.3) as per the Poisson effect. The load and axial displacement measurements were recorded by the RSA III and were used, together with the initial cross-sectional area of the specimen to determine the average axial stress and engineering strain. Figure 8.4 shows the compressive stress-strain data for the experiment conducted on

Specimen 1, as well as a linear regression line fit to the data. The linear regression was used to compute an estimate for E_1. The estimated value of $E_1 \approx 2.3$ MPa.

8.3 UNIAXIAL COMPRESSION CREEP TESTS

A series of five, ninety-six hour long uniaxial compression creep tests were conducted using the RSA III and specimens 2 through 6 were sequentially used to determine the Relaxation Modulus, E_∞, and the effective extensional viscosity, η_e, of the sealant material. A compressive stress of 23.735 kPa was applied to each of specimens 2 through 6 at constant temperatures of 23, 28, 33, 38 and 43ºC, respectively, in order for time-temperature superposition (TTSP) to be performed; additional details regarding TTSP are presented in the following section. The grip displacement data for each of the five experiments was used to calculate the engineering compressive strain. The engineering compressive strain was then used to calculate the true compressive stress and true compressive strain for each experiment through the use of **Eq. (10)** and **Eq. (11)**, respectively. The computed true compressive stresses in terms of time for each temperature are shown in Figure 8.5a, while true compressive strains in terms of time are shown in Figure 8.5b.

$$\sigma_t(t) = \sigma(t) \cdot \left(1 + \varepsilon(t)\right) \tag{10}$$

$$\varepsilon_t(t) = ln\left(1 + \varepsilon(t)\right) \tag{11}$$

8.4 TIME-TEMPERATURE SUPERPOSITION

The expression shown below in **Eq. (12)** (Williams et al. 1955) is the Williams-Landel-Ferry (WLF) equation which is frequently used to apply TTSP to experimental data in order to obtain results for an experiment which could last a long period of time by combining several shorter experiments at different temperatures. For the series of

experiments performed in this thesis, the WLF equation is used to obtain true compressive strains and true compressive stresses over the duration of the creep life of the sealant material. In this case, it should be possible to obtain a strain-time curve for the duration of the creep life of the asphalt sealant. The equation has been shown to be capable of being used with asphalt cements (Anderson et al. 1991) and was effectively used by Zhao (Zhao et al. 2003) to shift data from various temperatures. Furthermore, **Eq. (12)** can be rearranged into form shown in **Eq. (13)**, which can be used to determine constants D_1 and D_2 and therefore allow for the computation of $\log a_T$ for any temperature T with respect to T_{ref}.

$$\log \frac{t_{T_{ref}}}{t_T} = \log a_T = -\frac{D_1\left(T - T_{ref}\right)}{D_2 + \left(T - T_{ref}\right)} \tag{12}$$

$$\frac{-1}{\log a_T} = \frac{D_2}{D_1\left(T - T_{ref}\right)} + \frac{1}{D_1} \tag{13}$$

As stated in **Eq. (12)**, the ratio of times must first be converted to logarithmic time for time temperature superposition using WLF to be performed; 23ºC was used as the reference temperature, T_{ref}, during the shifting process. True compressive stresses and true compressive strains are shown as functions of logarithmic time in Figures 8.6a and Figure 8.6b, respectively. During each shift, approximately 84 % of source data set was shifted to the target data set, with the results used in the shifting selected from the latter portion of the latter portion of each experiment. The superposition was performed by first shifting data from 28ºC to 23ºC. The data from 33ºC was then shifted to the combined data set resulting from the shift of 28ºC data to 23ºC. The data from 38ºC was then shifted to the combined data set resulting from the previous shift. Finally, data from 43ºC was shifted to

the combined data set resulting from the shift of 38ºC data to 23ºC. The results of the four shifts performed for true compressive strain data are shown in Figures 8.7a to 8.7d, respectively, while the final combined true compressive stress and strain curves in terms of logarithmic time are shown in Figures 8.8a and 8.8b, respectively. The true compressive stress and true compressive strain in terms of time after the shifts are shown in Figures 8.9a and 8.9b, respectively. Through the use of TTSP, the amount of data available for the shingle sealant material at 23ºC was increased from 96 hours to 10.6 years.

All logarithmic shift factors, $\log a_T$, used in TTSP for compression creep data are listed in Table 8.2. Furthermore, in order to determine the constants D_1 and D_2 used in **Eq. (12)**, values of $-1/\log a_T$ were plotted as a function of $1/(T - T_{ref})$ and a linear regression line was fit through the resulting points (shown in Figure 8.10), as per **Eq. (13)**. The intercept of the resulting line was used to calculate D_1, the value of which was estimated to be 1.27, while the slope of the line and D_1 were used to calculate D_2, the value of which was estimated to be -24.08 ºC.

8.5 VISCOELASTIC ENERGY RELEASE RATE

The true compressive strains after TTSP, shown in Figure 8.9a, were combined with their respective true compressive strains after TTSP, shown in Figure 8.9b, in order to create the true stress-strain curve shown in Figure 8.11. A second order polynomial, shown in Figure 8.11, was fit to the data and was integrated from the initial to the final experimental strain under the assumption that the specimen would immediately fail if it was subjected to creep loading any longer. As per **Eq. (9)**, the value resulting from the integration was then multiplied separately by the heights of the shortest specimen

(Specimen 6 with a height of 12.840 mm) and the tallest specimen (Specimen 5 with a height of 13.496 mm) in order to obtain the lower and upper bounds, respectively, of the critical viscoelastic energy release rate, G_c. The approximate values of the lower and upper bounds were calculated to be 283.25 J/m^2 and 297.72 J/m^2.

8.6 RELAXED MODULUS AND YOUNG'S MODULUS OF SECOND LINEAR ELASTIC DAMPER

The value of the Relaxed Modulus, E_∞, was determined by dividing the constant compressive stress, σ_0 (23,735 Pa), by the average of the last 10 compressive strain values (0.93), as per **Eq. (7)**, resulting in a value of 26.1 kPa. The Young's Modulus, E_2, of the linear-elastic damper in the Kelvin Voigt unit (Figure 7.1), was determined to be 26.4 kPa.

8.7 EFFECTIVE EXTENSIONAL VISCOSITY

Several polynomial functions continuous at the boundary between regions were fitted to the true compressive strain data at 23ºC obtained through TTSP, as no one function was enough to encompass the entire data set. The functions for strain were then differentiated to obtain the compressive true strain rate. Subsequently, the true compressive stress data was divided by the corresponding strain rates obtained from the strain functions, as per **Eq. (1)**, in order to obtain values of effective extensional viscosity, η_e, at 23ºC. The calculated viscosities over the course of the five hours of experimentation, as well as a function for calculating the extension obtained from a sixth order polynomial fit to the data (chosen for having the best correlation out of the polynomial orders available), appear in Figure 8.12a. The calculated viscosity values for the entirety of the data after TTSP, with the corresponding sixth order polynomial fit, appear in Figure 8.12b. The 6th order polynomial fit shown in Figure 8.12 was used to estimate the values of η_e(1 hr.) and η_e(5

hrs.), resulting in quantities of $3.15 \cdot 10^9$ Pa·s and $6.49 \cdot 10^9$ Pa·s, respectively. All material properties of the shingle sealant calculated from experimental data appear in Table 8.3.

Table 8.1 Dimensions of shingle sealant material specimens used for testing

Specimen	**Height (mm)**	**Diameter (mm)**
Specimen 1	13.390	14.996
Specimen 2	13.346	15.001
Specimen 3	13.332	14.971
Specimen 4	13.272	15.065
Specimen 5	13.496	14.978
Specimen 6	12.840	15.156

Table 8.2 Values of the logarithm of the shift factor at various testing temperatures

Temperature (ºC)	$\mathbf{log}(\boldsymbol{a_T})$	$\boldsymbol{log(t_T)}$	$\boldsymbol{T_{ref}}$ **(ºC)**
28	0.326	5.181	23
33	1.116	4.722	23
38	2.291	4.330	23
43	2.984	4.799	23

Table 8.3 Properties of shingle sealant material computed from experimental data

Property	**Experimental Value**
E	279 MPa
E_1	2.3 MPa
E_∞	26.1 kPa
E_2	26.4 kPa
η_e(1 hour)	$3.15 \cdot 10^9$ Pa·s
η_e(5 hours)	$6.49 \cdot 10^9$ Pa·s

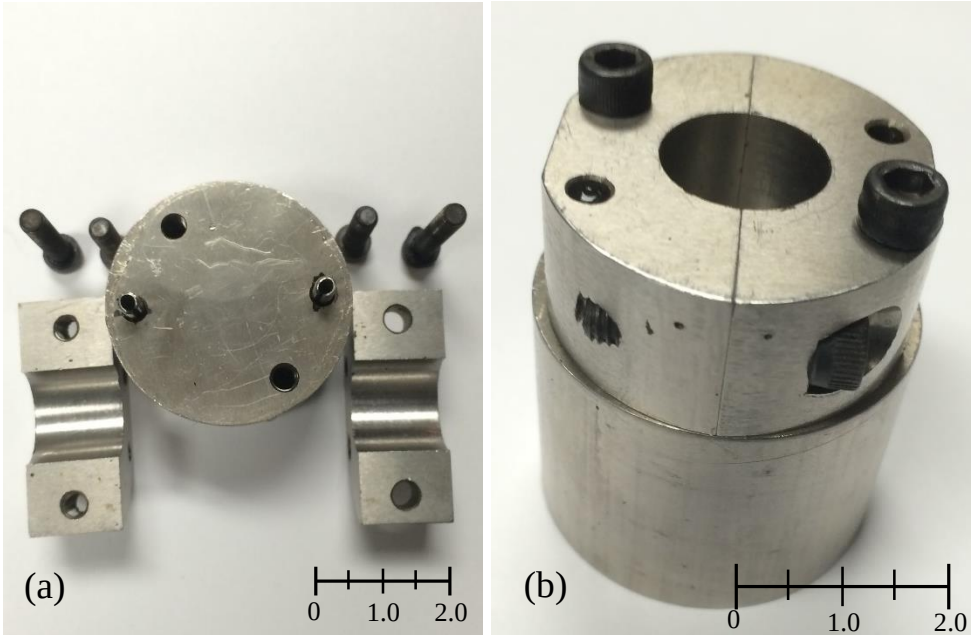

Figure 8.1 Stainless steel mold used for manufacturing specimens from shingle sealant material in: (a) disassembled form; and (b) assembled form. Ruler units in centimeters.

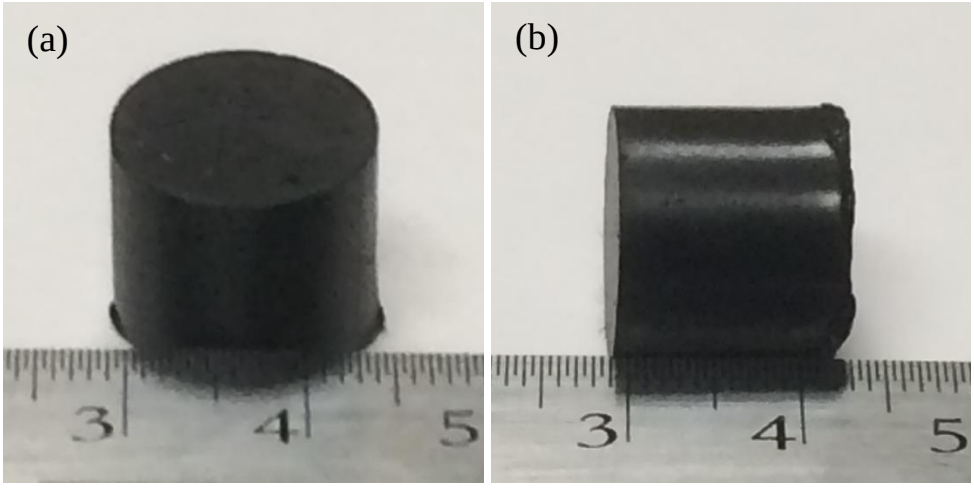

Figure 8.2 Shingle sealant material Specimen 1: (a) front view; and (b) side view. Ruler units in centimeters.

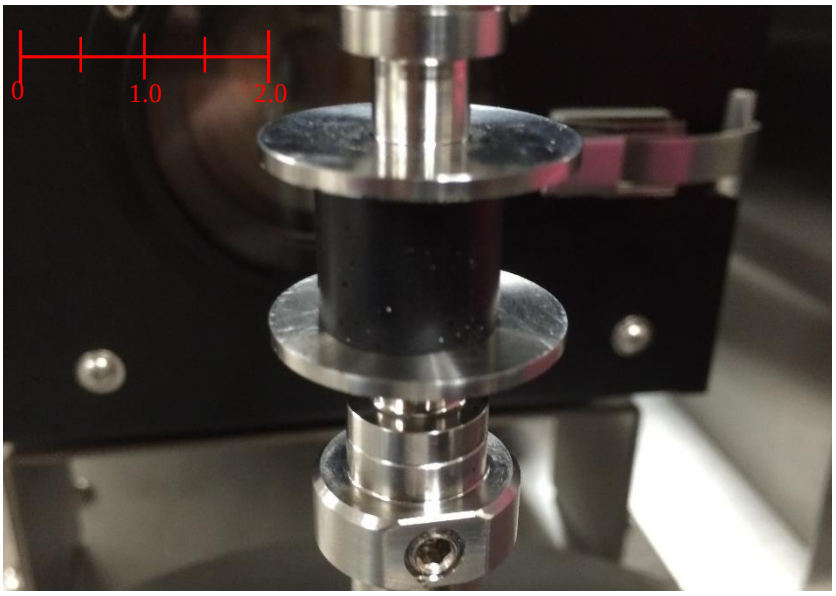

Figure 8.3 Cylindrical specimen composed of sealant strip material in between steel platens of RSA III test system. As the specimen is compressed, the diameter of the specimen grows outward towards the edges of the platens. Ruler units in centimeters.

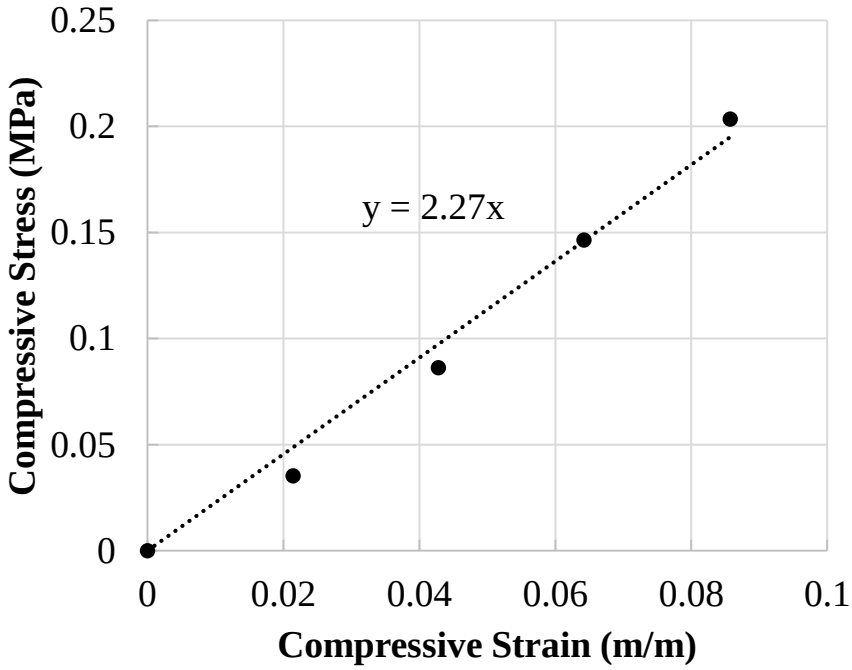

Figure 8.4 Experimental compressive stress-strain response of sealant specimen shown in Figure 8.2 (obtained at temperature of 23°C).

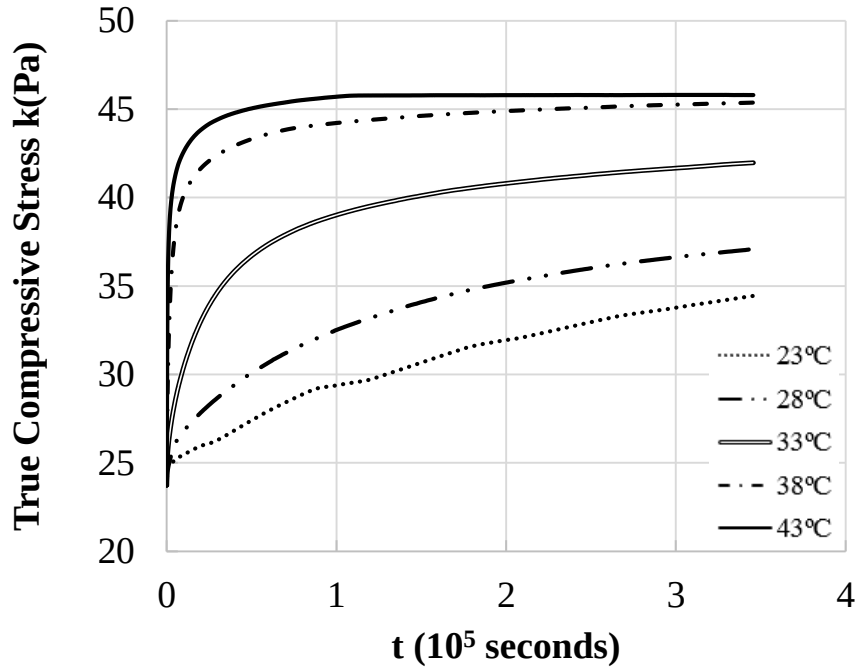

(a)

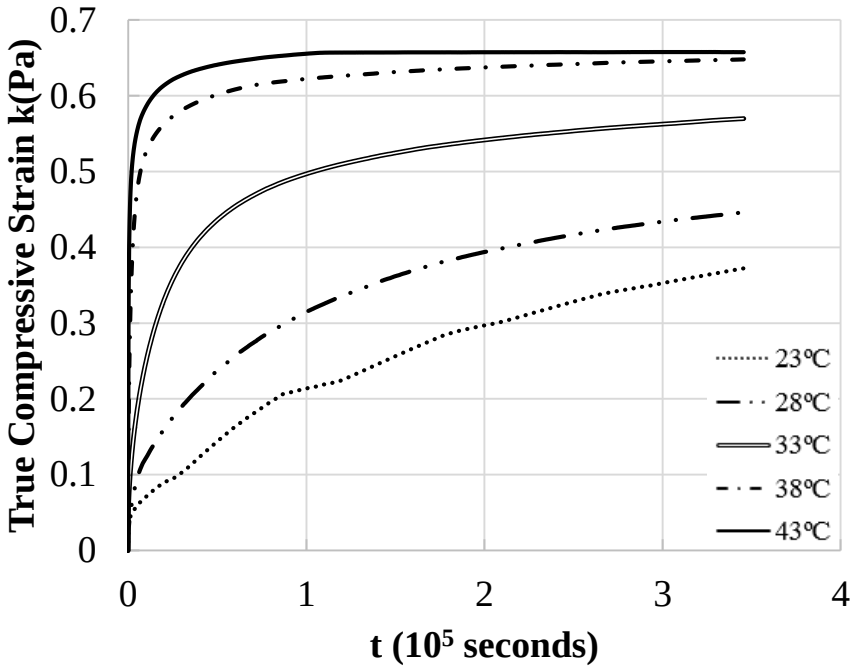

(b)

Figure 8.5 (a) True compressive stress response; and (b) true compressive strain response, as a function of time, of Specimens 2-6 loaded with a constant compressive stress of 23,735 Pa at temperatures of 23, 28, 33, 38 and 43ºC respectively.

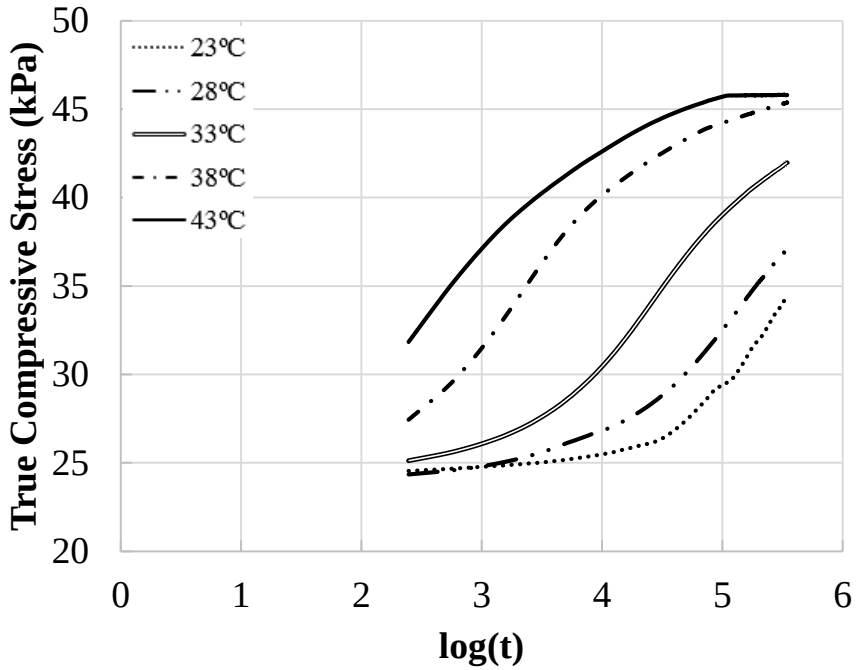

(a)

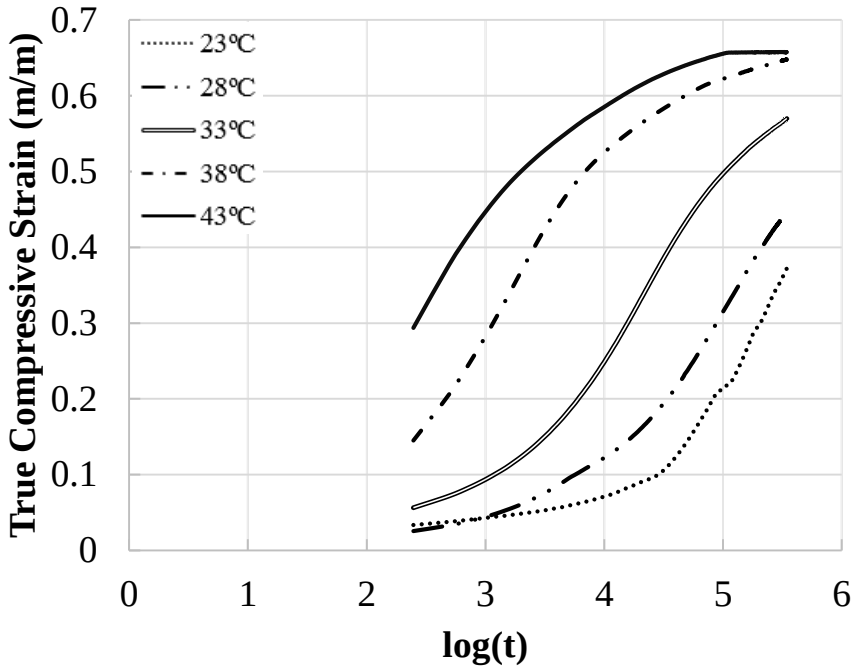

(b)

Figure 8.6 (a) True compressive stress response; and (b) true compressive strain response, as a function of logarithmic time, of Specimens 2-6 loaded with a constant compressive stress of 23,735 Pa at temperatures of 23, 28, 33, 38 and 43ºC, respectively. The units of t are seconds.

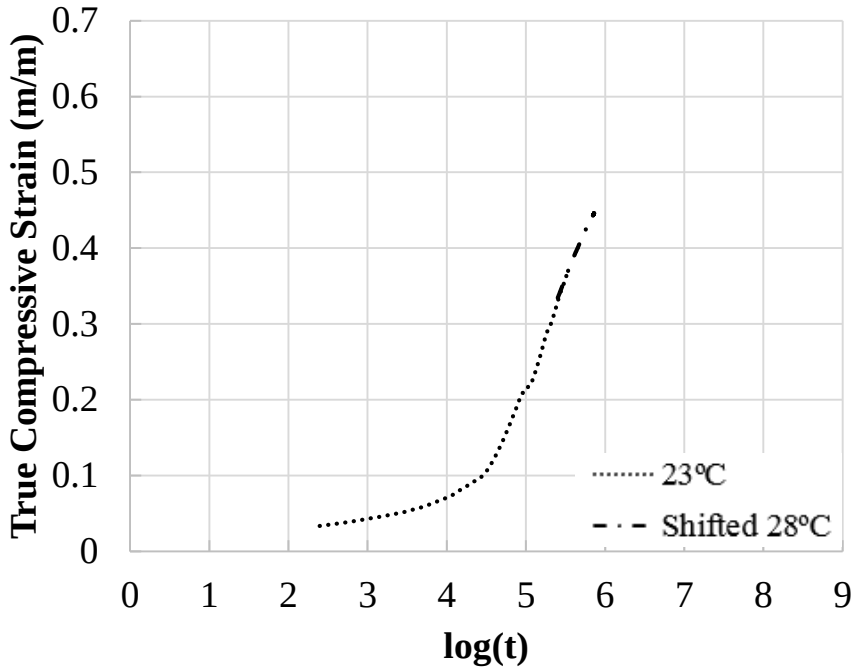
True Compressive Strain (m/m)
0.7
0.6
0.5
0.4
0.3
0.2
0.1
0
0 1 2 3 4 5 6 7 8 9
log(t)
23ºC
Shifted 28ºC

(a)

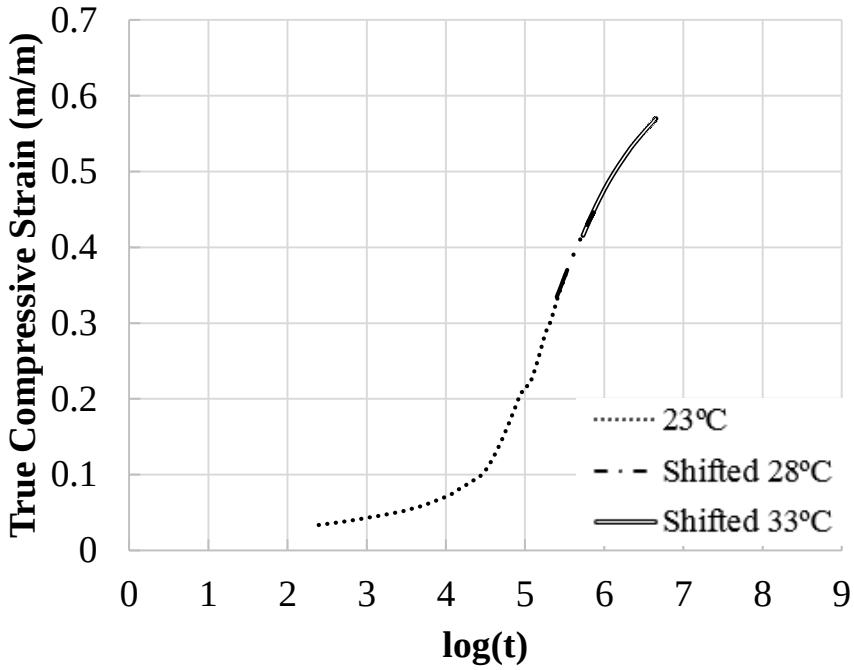
True Compressive Strain (m/m)
0.7
0.6
0.5
0.4
0.3
0.2
0.1
0
0 1 2 3 4 5 6 7 8 9
log(t)
23ºC
Shifted 28ºC
Shifted 33ºC

(b)

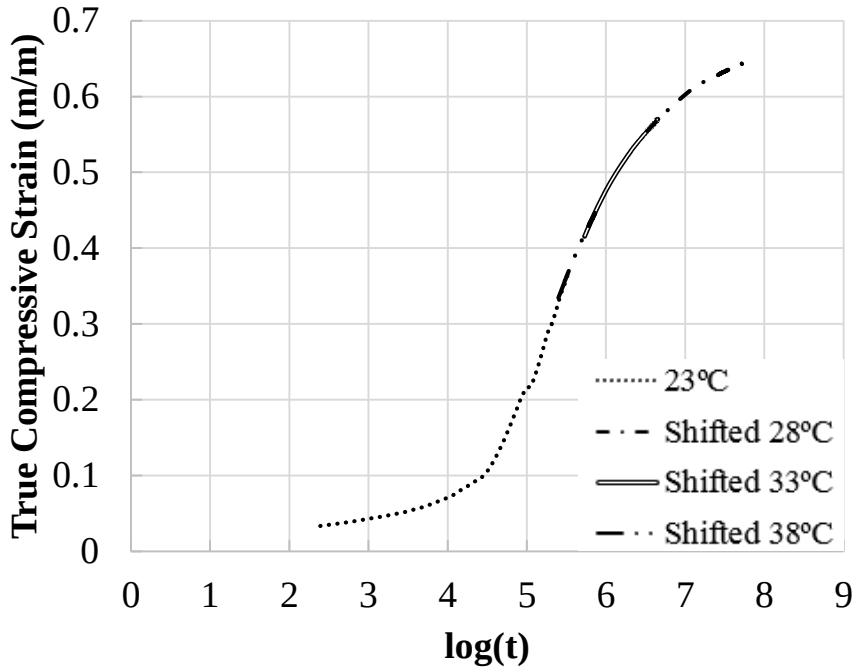

(c)

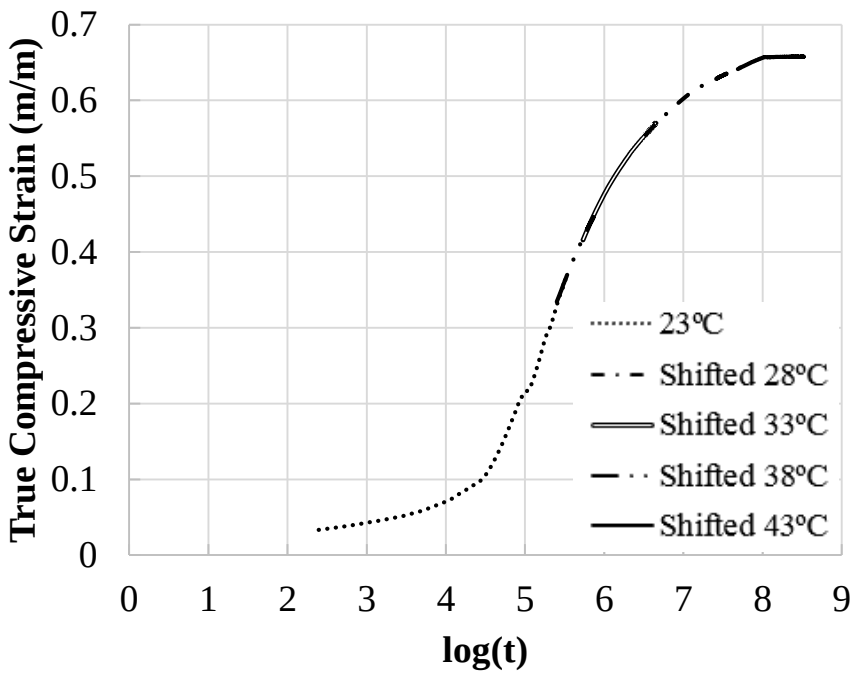

(d)

Figure 8.7 TTSP shifts of true compressive strain data from (a) 28 to 23ºC; (b) 33ºC to the 23ºC data extended by the shift of 28ºC data; (c) 38ºC to the 23ºC data extended by the shift of 28 and 33ºC data; (d) 43ºC to the 23ºC data extended by the shift of 28, 33 and 43ºC data. The units of t are seconds.

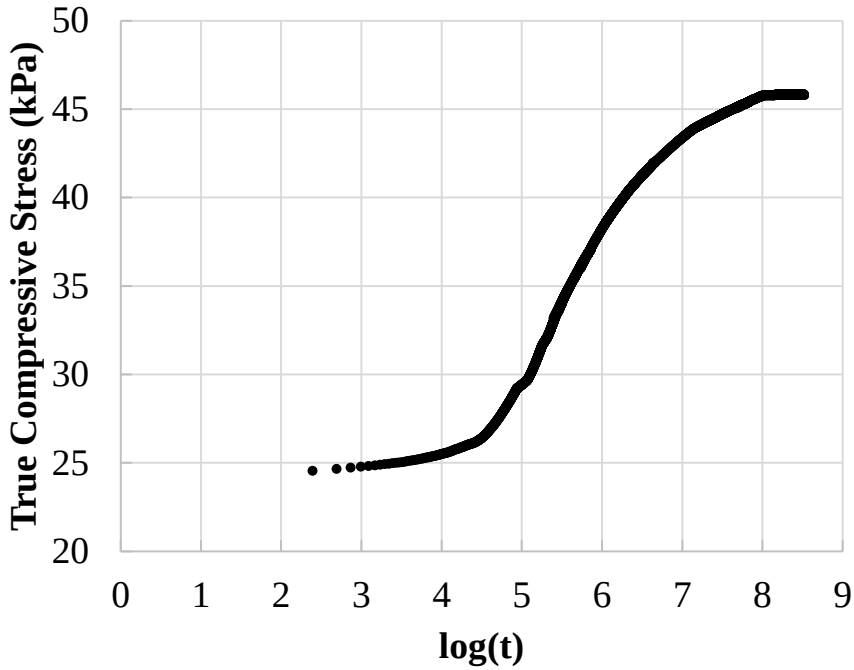

(a)

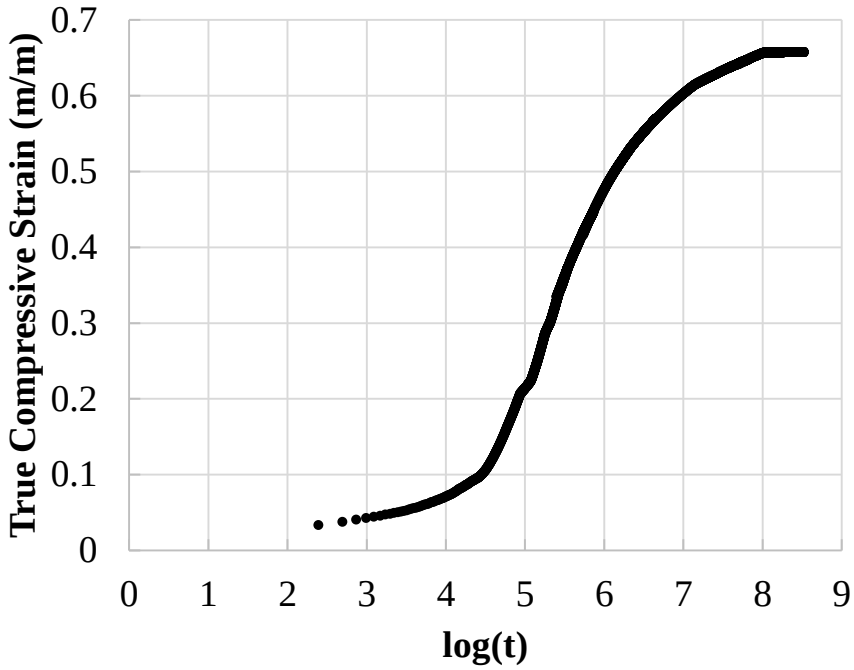

(b)

Figure 8.8 True compressive (a) stress; and (b) strain; response of shingle sealant material at 23ºC and under a constant compressive stress of 23,735 Pa after TTSP as functions of logarithmic time. The units of t are seconds.

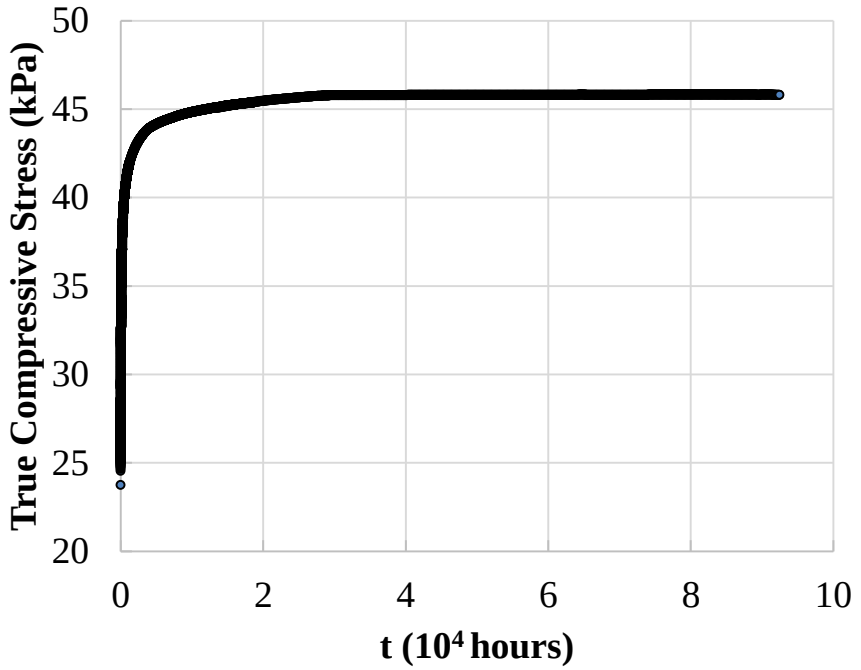

(a)

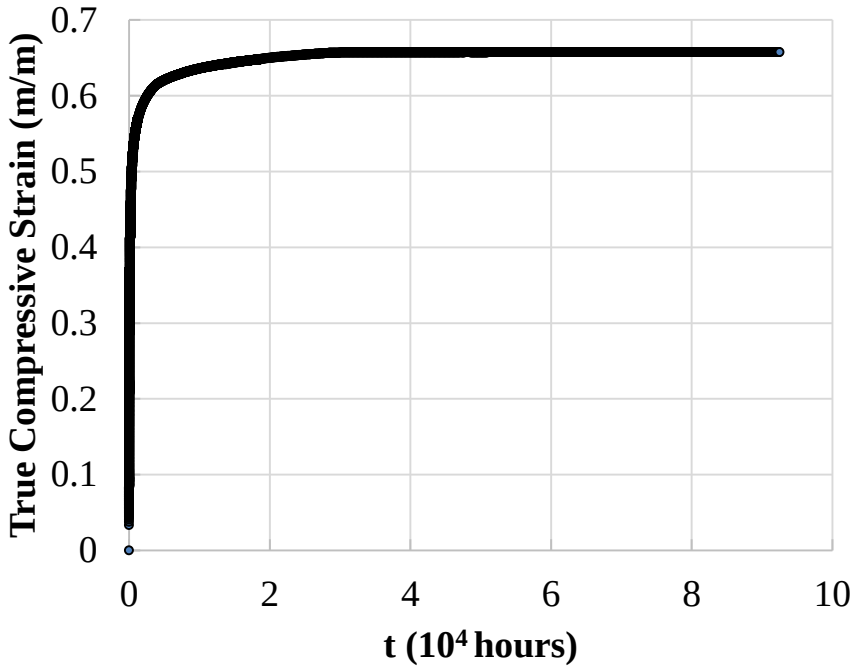

(b)

Figure 8.9 True compressive (a) stress; and (b) strain; response of shingle sealant material at 23ºC and under a constant compressive stress of 23,735 Pa after TTSP.

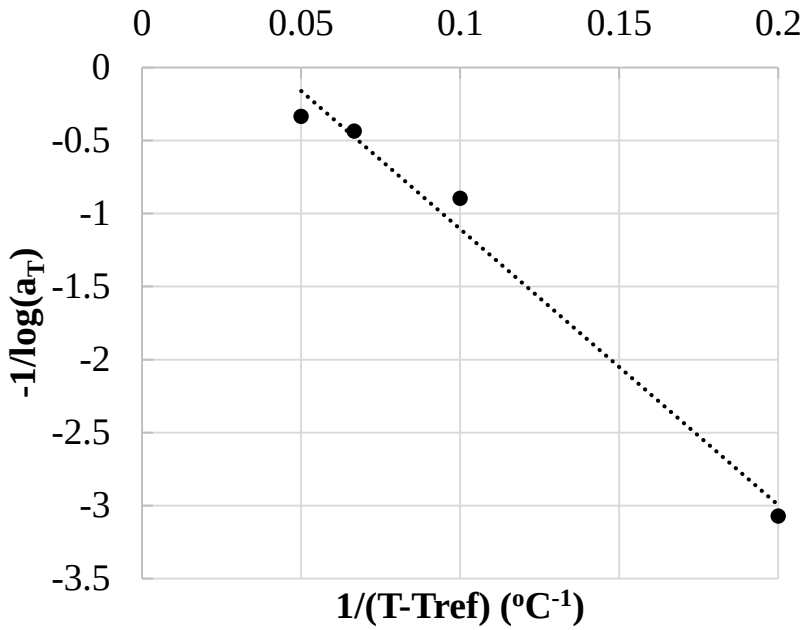

Figure 8.10 Plot of $-1/\log a_T$ as a function of $1/(T - T_{ref})$ as well as the linear regression line used for the calculation of WLF constants D_1 and D_2, as per **Eq. (13)**. Functional fit is written y = -18.917x + 0.7856.

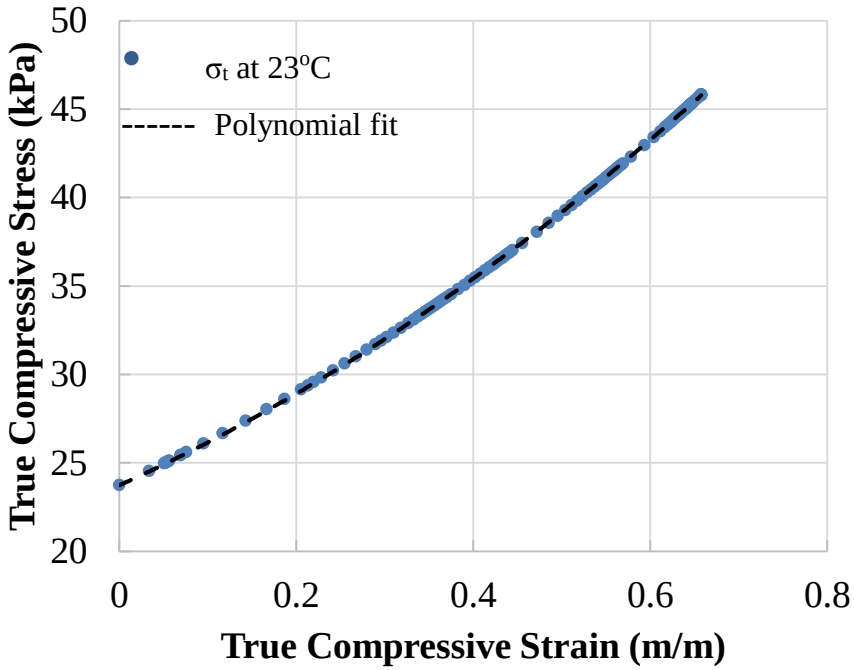

Figure 8.11 True compressive stress-strain data (obtained from the combination of data in Figure 8.9) and second order polynomial fit. Functional fit is written $y = 16.690x^2 + 22.550x + 23.735$ with $R^2 = 1.000$.

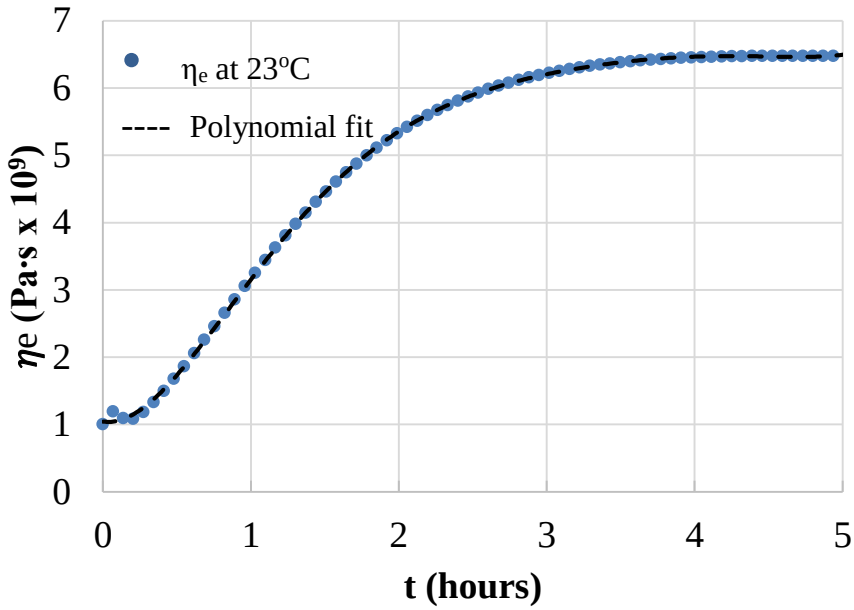

(a)

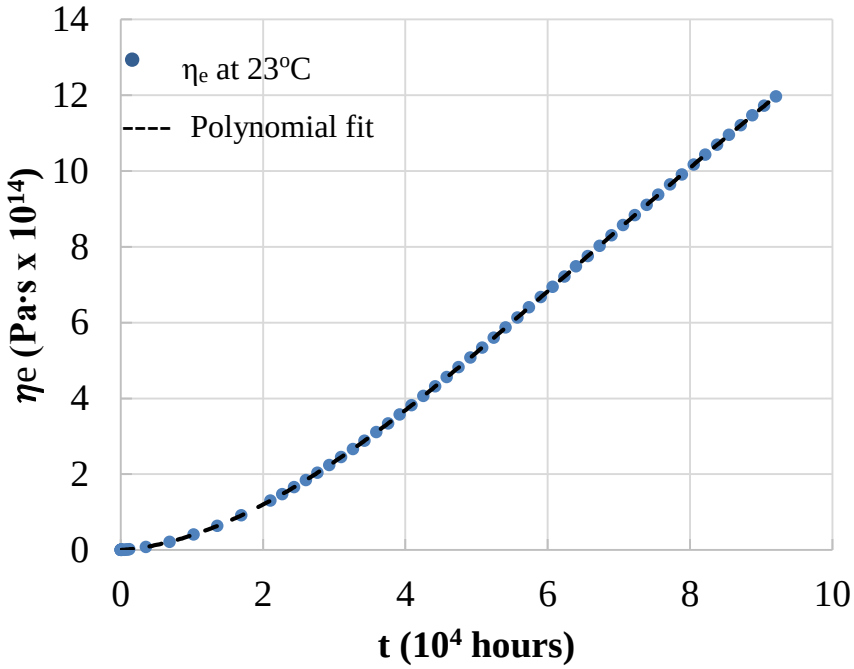

(b)

Figure 8.12 Effective extensional viscosity of shingle sealant material over the course of: (a) 5 hours with polynomial fit $y = 6.50E+06x^6 - 1.18E+08x^5 + 8.50E+08x^4 - 2.95E+09x^3 + 4.51E+09x^2 - 1.40E+08x + 1.00E+09$ and $R^2 = 1.00E+00$; (b) 92,477 hours with $y = 1.16E-15x^6 - 3.05E-10x^5 + 3.37E-05x^4 - 3.16E+00x^3 + 2.88E+05x^2 + 1.28E+09x + 1.00E+09$ and $R^2 = 1.00E+00$.

CHAPTER 9

FINITE ELEMENT ANALYSIS STUDIES OF SHINGLE-SEALANT STRUCTURAL RESPONSE

The mechanical schematics of single and double adhesive strip one-layer asphalt roof shingle systems are shown in Figures 9.1a and 9.1b, respectively. Throughout the analysis, it is assumed, as per Croom et al. 2015a, that the shingle as well as the sealant have unit width in the z-direction (orthogonal to *x* and *y* in Figure 9.1). Furthermore, it is assumed that the pressure distribution of the loading does not change with time. A list of the BOEF model parameters, notations, and dimensional units used in this portion of the thesis appears in Table 9.1.

The single sealant shingle of length $l^s = l_1^s + l_2^s + l_3^s$, shown in Figure 9.1a, is modeled using several BEAM189 three-dimensional elements in ANSYS 15.0 (Figure 9.2), with a width dimension of *w*, height dimension of *h*, and a modulus of elasticity of *E*. Regions 1s, 2s and 3s have areas of A_1^s, A_2^s and A_3^s, and are meshed into e_1^s, e_2^s and e_3^s BEAM 189 elements, respectively, with each region containing n_1^s, n_2^s and n_3^s nodes. The loading on the shingle is provided by two series of constant forces F_1^s and F_3^s which are applied between the nail line and the inner edge of the sealant strip and between the outer edge of the sealant strip and the end of the shingle. The values of F_1^s and F_3^s can be calculated from **Eq. (14a)** and **(14b)**, where p_1^s and p_3^s are pressures applied to Regions 1s and 3s.

$$F_1^s = \frac{p_1^s A_1^s}{n_1^s} \tag{14a}$$

$$F_3^s = \frac{p_3^s A_3^s}{n_3^s} \tag{14b}$$

The double sealant shingle of length $l^d = l_1^d + l_2^d + l_3^d + l_4^d + l_5^d$, shown in Figure 9.1b, is also modeled using BEAM189 three-dimensional elements (Figure 9.3) with a width dimension of *w*, height dimension of *h*, and a modulus of elasticity of *E*. Regions 1d, 2d, 3d, 4d and 5d have areas of A_1^d, A_2^d, A_3^d, A_4^d and A_5^d, and are meshed into e_1^d, e_2^d, e_3^d, e_4^d and e_5^d BEAM 189 elements, respectively, with each region containing n_1^d, n_2^d, n_3^d, n_4^d and n_5^d nodes. Throughout the thesis, the lengths of the single sealant shingle and the double sealant shingle remain constant and equal such that $l = l^s = l^d$. The loading on the double sealant shingle is provided by three series of constant forces F_1^d, F_3^d and F_5^d which are applied between the nail line and the inner edge of the inner sealant strip, between in the outer edge of the inner sealant strip and the inner edge of the outer sealant strip and between the outer edge of the outer sealant strip and the end of the shingle, respectively. The values of F_1^d, F_3^d and F_5^d can be calculated from **Eqns. (15a), (15b)** and (**15c)**, where p_1^d, p_3^d and p_5^d are pressures applied to Regions 1d, 3d and 5d, respectively.

$$F_1^d = \frac{p_1^d A_1^d}{n_1^d} \tag{15a}$$

$$F_3^d = \frac{p_3^d A_3^d}{n_3^d} \tag{15b}$$

$$F_5^d = \frac{p_5^d A_5^d}{n_5^d} \tag{15c}$$

The sealant strip in the single strip model of length l_2^s, as well as the inner and outer sealant strips in the double sealant model of lengths l_2^d and l_4^d, are modeled as a series of LINK180 link elements. Given that the sealant strip length was not varied between the models, the following equalities are in effect for the lengths of Regions 2s, 2d and 4d: $l_2^s = l_2^d = l_4^d$, $e_2^s = e_2^d = e_4^d$ and $n_2^s = n_2^d = n_4^d$. Furthermore, since LINK180 elements are attached to the nodes of BEAM189 elements in Regions 2s, 2d and 3d, the total number of LINK180 elements modeling each sealant strip is $n_2^s = n_2^d = n_4^d$. Each LINK180 element has an area of A^l, which can be obtained from **Eq. (16)**, and a thickness of a.

$$A^l = \frac{A_2^s}{n_2^s} = \frac{A_2^d}{n_2^d} = \frac{A_4^d}{n_4^d} \tag{16}$$

Four different models were created in order to simulate the structural response of shingle-sealant systems with respect to 150 mph 3-s gusts. Models S1 and S2 simulate the response of the single shingle-sealant system (Figure 9.1a, Figure 9.2) subjected to 150 mph 3-s gusts for one hour and five hours, respectively. Models D1 and D2 simulate the response of the double shingle- sealant system (Figure 9.1b, Figure 9.3) subjected to 150 mph 3-s gust for one hour and five hours, respectively.

The values of the dimensions used for the single sealant models (Models S1 and S2) are listed in Table 9.2, while the values of the dimensions used for the double sealant models (Models D1 and D2) appear in Table 9.3. In addition, the element and node counts for both the single and double sealant models are listed in Table 9.4. From Croom et al.

2015b, it is known that the pressures acting upon Models S1 and S2 are p_1^s = 507 Pa and p_3^s = 2028 Pa, while from the previous portion of the thesis, it is known that the pressures acting upon Models D1 and D2 are p_1^d = p_3^d = 507 Pa and p_5^d = 2028 Pa. The pressures p_1^s and p_3^s were used with **Eq. (14a)** and (**14b)** in order to calculate the forces F_1^s and F_3^s acting on Regions 1s and 3s, respectively, of the single sealant asphalt shingle (Figure 9.1a) The pressures p_1^s, p_3^s and p_5^s were used with **Eqns. (15a), (15b)** and **(15c)** in order to calculate the forces F_1^s, F_3^s and F_5^s acting on Regions 1d, 3d and 5d, respectively, of the double sealant asphalt shingle (Figure 9.1b). The calculated values of the forces applied to both the single and double sealant models appear in Table 9.5.

Figures 9.2 and 9.3 show the as-developed finite element models for the single and double-sealant cases, respectively. Each of the four FEA models described above simulated its designated amount of time (1 hour for Models S1 and D1 and 5 hours for Models S2 and D2), after which the stress and strain data at the edges of the sealants of the models (locations x = $l_1^s, l_1^s + l_2^s$ in Figure 9.1a for Models S1 and S2; locations x = $l_1^d, l_1^d + l_2^d, l_1^d + l_2^d + l_3^d$ and $l_1^d + l_2^d + l_3^d + l_4^d$ in Figure 9.1b for Models D1 and D2) was extracted and converted to true stress and true strain, respectively. Second order polynomials were used to establish the correlations between each set of true stress and true strain data and were subsequently used with the thickness of the sealant, *a*, and **Eq. (9)** to determine the viscoelastic energy release rates, *G*, at each sealant edge for the duration of the simulations.

Table 9.1 Asphalt roof shingle-sealant FEA model parameters and dimensional units.

Notation	**Parameter**	**Dimensional unit**[4]
l	Length of shingle (along axis *x*)	L
l^s	Length of single sealant strip shingle (along axis *x*)	L
l^d	Length of double sealant strip shingle (along axis *x*)	L
l_1^s	Distance between nail line and inner edge of sealant strip of single sealant strip shingle(along axis *x*)	L
l_2^s	Length of sealant strip of single sealant strip shingle (along axis *x*)	L
l_3^s	Length of leading edge of single sealant shingle (along axis *x*)	L
l_1^d	Distance between nail line and inner edge of inner sealant strip (along axis *x*)	L
l_2^d	Length of inner sealant strip (along axis *x*)	L
l_3^d	Distance between outer edge of inner sealant strip and inner edge of outer sealant strip (along axis *x*)	L
l_4^d	Length of outer sealant strip (along axis *x*)	L
l_5^d	Length of leading edge of shingle (along axis *x*)	L
w	Width of shingle material (along axis *z*)	L
H	Height of shingle material (along axis *y*)	L
A_1^s	Area of Region 1s of single sealant shingle (with normal axis *y*)	L^2
A_2^s	Area of Region 2s of single sealant shingle (with normal axis *y*)	L^2
A_3^s	Area of Region 3s of single sealant shingle (with normal axis *y*)	L^2
A_1^d	Area of Region 1d of double sealant shingle (with normal axis *y*)	L^2

[4] F = force; L = length; T = time.

A_2^d	Area of Region 2d of double sealant shingle (with normal axis *y*)	L^2
A_3^d	Area of Region 3d of double sealant shingle (with normal axis *y*)	L^2
A_4^d	Area of Region 4d of double sealant shingle (with normal axis *y*)	L^2
A_5^d	Area of Region 5d of double sealant shingle (with normal axis *y*)	L^2
A^l	Area of LINK180 element. (with normal axil y)	L^2
a	Thickness of the sealant	L
E	Elastic modulus of shingle material	FL^{-2}
E_1	Elastic modulus of sealant material	FL^{-2}
E_∞	Relaxation modulus of sealant material	FL^{-2}
E_2	Elastic modulus of linear damper of Kelvin Voigt in Standard Linear model for sealant material	FL^{-2}
η_e	Effective extensional viscosity of sealant material	FTL^{-2}
p_1^s	Out-of-plane surface pressure on shingle surface between nail line and inner edge of sealant strip of single sealant shingle	FL^{-2}
p_3^s	Out-of-plane surface pressure on single sealant shingle leading edge of single sealant shingle	FL^{-2}
F_1^s	Out-of-plane surface force applied to nodes of shingle surface between nail line and inner edge of sealant strip of single sealant shingle	F
F_3^s	Out-of-plane surface force applied to nodes of single sealant shingle leading edge of single sealant shingle	F
p_1^d	Out-of-plane surface pressure on shingle surface between nail line and inner edge of inner sealant strip of double sealant shingle	FL^{-2}
p_3^d	Out-of-plane surface pressure on shingle surface between outer edge of inner sealant strip and inner edge of outer sealant strip of double sealant shingle	FL^{-2}
p_5^d	Out-of-plane surface pressure on shingle leading edge of double sealant shingle	FL^{-2}

F_1^s	Out-of-plane surface force applied to nodes of shingle surface between nail line and inner edge of inner sealant strip of double sealant shingle	F
F_3^s	Out-of-plane surface force applied to nodes of shingle surface between outer edge of inner sealant strip and inner edge of outer sealant strip of double sealant shingle	F
F_5^s	Out-of-plane surface force applied to nodes of shingle leading edge of double sealant shingle	F
G	Applied energy release rate at sealant strip edge	FL^{-1}

Table 9.2 Dimensions of Models S1 and S2.

Dimension	**Value**
l^s	0.1334 m
l_1^s	0.10244 m
l_2^s	0.0127 m
l_3^s	0.01826 m
w	1.00 m
H	0.002159 m
a	0.002794 m
A_1^s	0.10244 m^2
A_2^s	0.0127 m^2
A_3^s	0.01826 m^2
A^l	1.233E-4 m^2

Table 9.3 Dimensions of Models D1 and D2.

Dimension	**Parameter**
l^d	0.1334 m
l_1^d	0.0521 m
l_2^d	0.0127 m
l_3^d	0.0479 m

l_4^d	0.0127 m
l_5^d	0.008 m
w	1.00 m
H	0.002159 m
a	0.002794 m
A_1^d	0.0521 m^2
A_2^d	0.0127 m^2
A_3^d	0.0479 m^2
A_4^d	0.0127 m^2
A_5^d	0.008 m^2
A^l	1.233E-4 m^2

Table 9.4 Element (BEAM189) and node counts of FEA models.

Element Set	**Number of Elements**	**Node Set**	**Number of Nodes**
e_1^s	410	n_1^s	821
e_2^s	51	n_2^s	103
e_3^s	74	n_3^s	149
e_1^d	201	n_1^d	403
e_2^d	51	n_2^d	103
e_3^d	192	n_3^d	385
e_4^d	51	n_4^d	103
e_5^d	32	n_5^d	65

Table 9.5 Forces applied to single and double sealant FEA models.

Force	**Value**
F_1^s	0.063 N
F_3^s	0.248 N
F_1^d	0.063 N
F_3^d	0.063 N
F_5^d	0.250 N

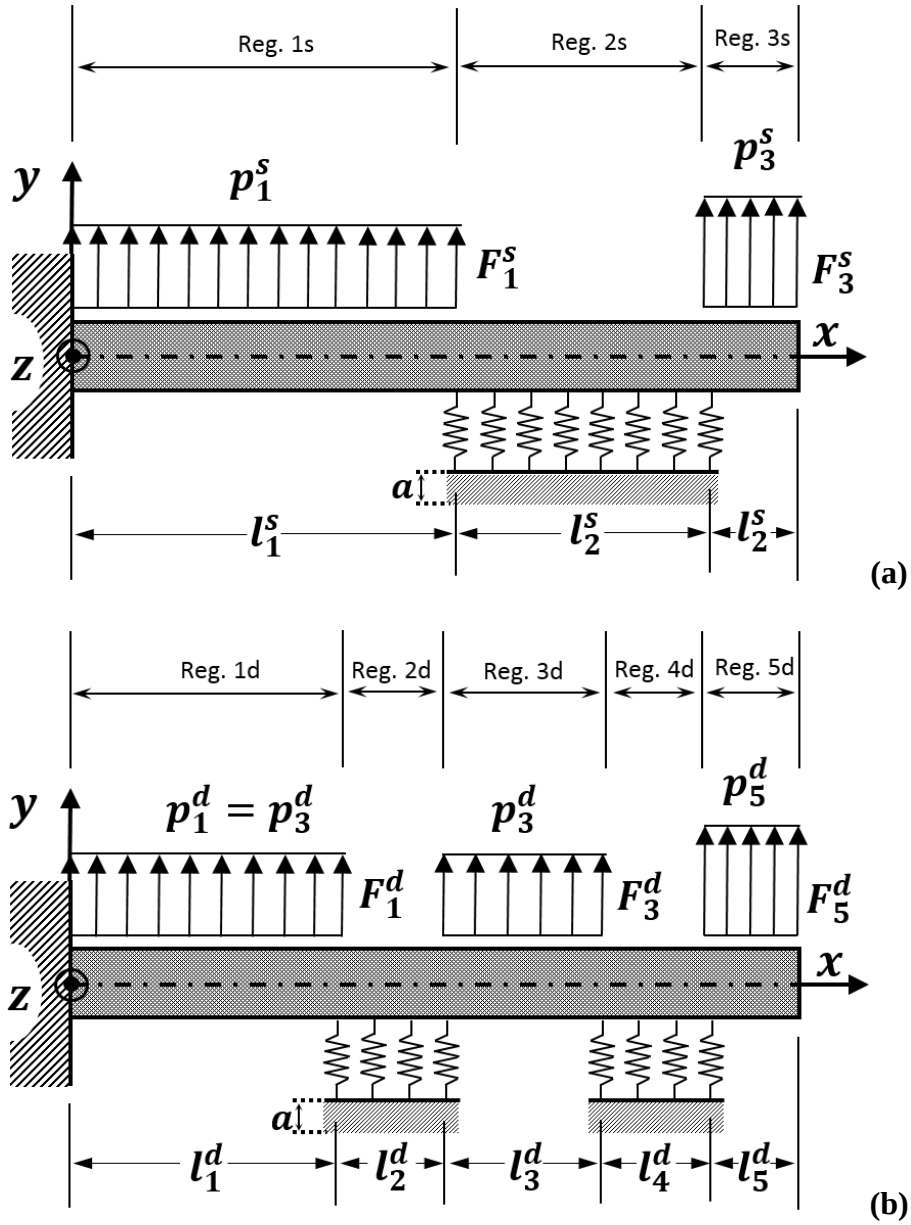

Figure 9.1 Structural model with loading and boundary conditions of (a) single sealant asphalt roof shingle-sealant system; and (b) double sealant asphalt roof shingle-sealant system. Note that axis *z* is perpendicular to axis *x* and *y* and springs denote a viscoelastic foundation.

Figure 9.2 Meshed geometries of single sealant Models S1 and S2 made up of Regions 1s (composed of e_1^s BEAM189 elements), 2s (composed of e_2^s BEAM189 elements and n_2^s LINK180 elements) and 3s (composed of e_3^s BEAM189 elements). The quantities of elements in each region are located in Table 9.4.

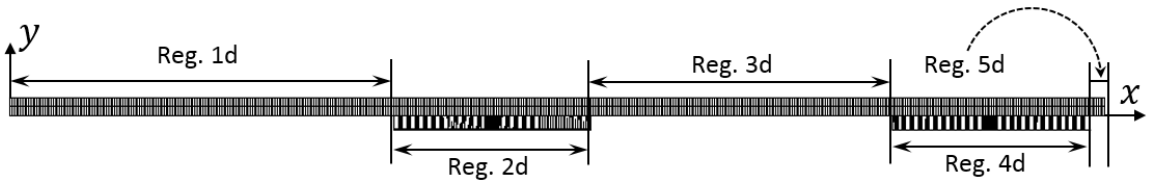

Figure 9.3 Meshed geometries of double sealant Models D1 and D2 made up of Regions 1d (composed of e_1^d BEAM189 elements), 2d (composed of e_2^d BEAM189 elements and n_2^s LINK180 elements), 3d (composed of e_3^d BEAM189 elements), 4d (composed of e_4^d BEAM189 elements and n_2^s LINK180 elements) and 5d (composed of e_5^d BEAM189 elements). The quantities of elements in each region are located in Table 9.4.

CHAPTER 10

RESULTS AND DISCUSSIONS OF VISCOELASTIC SIMULATIONS

The computed values of G for the inner and outer edges of the sealant for the duration of the simulations in single sealant Models S1 and S2 appear in Figure 10.1a and Figure 10.1b, respectively. Furthermore, Figures 10.2a and 10.2b show the stress and strain distributions at the final time of the simulation in single sealant Model S1. The computed values of G for the inner edge of the inner sealant, the outer edge of the inner sealant, the inner edge of the outer sealant and the outer edge of the outer sealant of the double sealant Models D1 and D2 appear in Figures 10.3a and 10.3b, respectively. Figure 10.4 contains a visual comparison of the greatest values of G, from each of the four models used, as well as the least and upper bounds of the experimentally estimated critical viscoelastic energy release rate, G_c. Furthermore, the values of G at the final time of Models S1 and S2 tabulated in Table 10.1 while the final values of G for Models D1 and D2 are tabulated in Table 10.2.

Several observations can be made from the simulation data. First, as shown in Figure 10.2, there are large gradients in the stresses and strains within each sealant layer, with the maxima occurring at the edges of each layer. Regarding the maximum values, the inner edge of the sealant always has the greatest value of G in Models S1 and S2, while the outer edge of the sealant always has a smaller value. Interestingly, a similar trend is observed for the two-sealant model when the pressures are maintained at their initial values. In this case, the inner edge of the inner sealant in Models D1 and D2 always has

the greatest value of G, while the outer edge of the outer shingle (i.e. the leading edge of the shingle) always has the smallest.

By comparing the final maximum values of G from Models S1 and D1, which occur at t =1 hour. It is evident that the value of G is slightly over 14 times larger for Model S1 and D1. Similarly, while comparing the maximum G results from Models S2 and D2, which occur at t =5 hours, it can be observed that the value of G from Model S2 is over 14 times larger than that of Model D2. It can be concluded from these observations that the double sealant model is clearly superior to the single sealant asphalt shingle system currently used in modern configurations.

From Figure 10.4, it can be concluded that neither the single nor double sealant shingle configurations modeled will fail after an hour of 150 mph 3-s gust as the maximum values of G from neither Model S1 or Model D1 reach the lower bounds of G_c computed from the post-TTSP true stress and true strain data. Furthermore, from the four simulations conducted, it appears that Model S2, the five hour single sealant model, is the only one to show that the shingle will fail, doing so in 4.1 hours if using the lower bound of G_c and 4.3 hours if using the upper bound of G_c.

With regard to the simulations, two limitations are noted. First, though the results indicating that the single sealant strip asphalt-shingle system will fail in 4.1 to 4.3 hours, are based on the use of engineering strain due to limitations of the beam element models in ANSYS which do not change cross sectional area during the course of the simulation and therefore do not use true stress or true strain.

Another limitation of the simulations is the observation that the viscosity term at

the final time was used in the predictions due to software limitations using the beam elements. In fact, the viscosity does not stay constant in the real world as it is affected by both stress and strain rate within the material. The value of the viscosities used is therefore the upper bound over the viscosity values over the time range of the simulation. A more accurate result can therefore be achieved if a model is made which accounts for true stress, true strain, and changing viscosity.

Table 10.1 Final values of *G* at the edges of the sealant in Models S1 and S2.

	Model S1	**Model S2**
Inner Edge of Sealant Strip	152.01 J/m^2	338.39 J/m^2
Outer Edge of Sealant Strip	111.10 J/m^2	235.97 J/m^2

Table 10.2 Final values of *G* at the edges of the sealants in Models D1 and D2.

	Model D1	**Model D1**
Inner Edge of Inner Sealant Strip	10.67 J/m^2	23.62 J/m^2
Outer Edge of Inner Sealant Strip	8.55 J/m^2	18.46 J/m^2
Inner Edge of Outer Sealant Strip	8.52 J/m^2	18.45 J/m^2
Outer Edge of Outer Sealant Strip	5.57 J/m^2	11.25 J/m^2

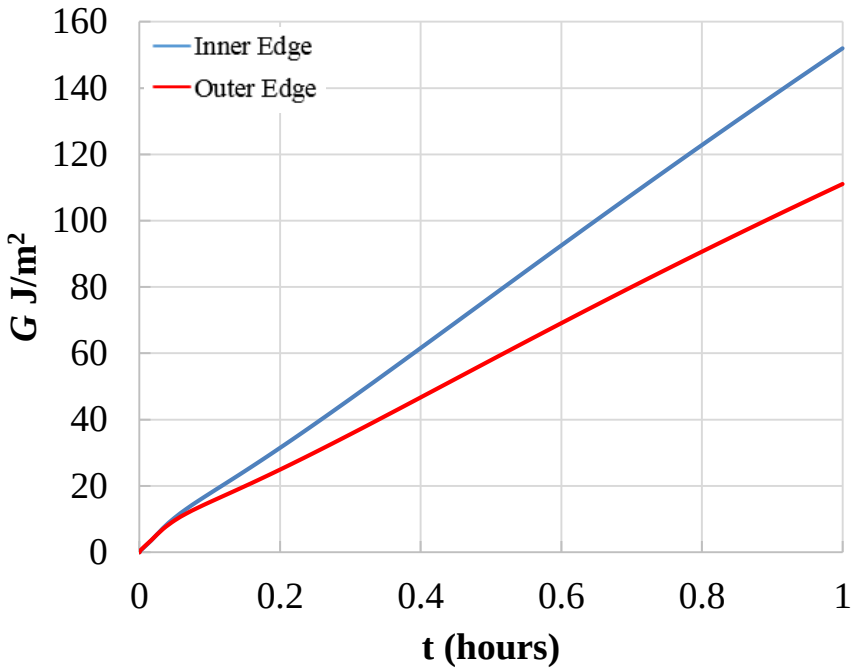

(a)

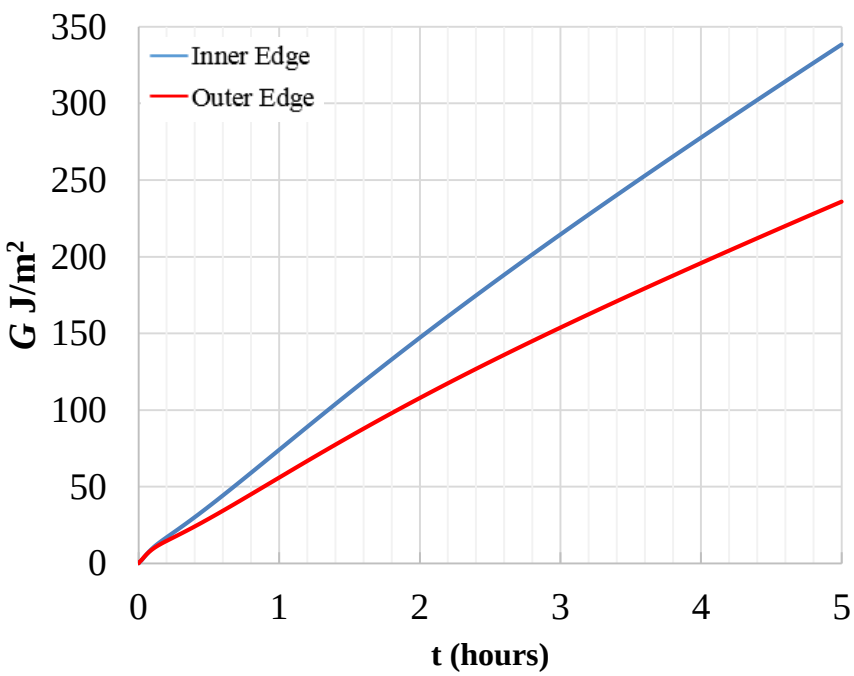

(b)

Figure 10.1 Applied energy release rate, *G*, at the inner and outer edges of the sealant for the duration of the simulations in (a) single sealant Model S1; and (b) single sealant Model S2.

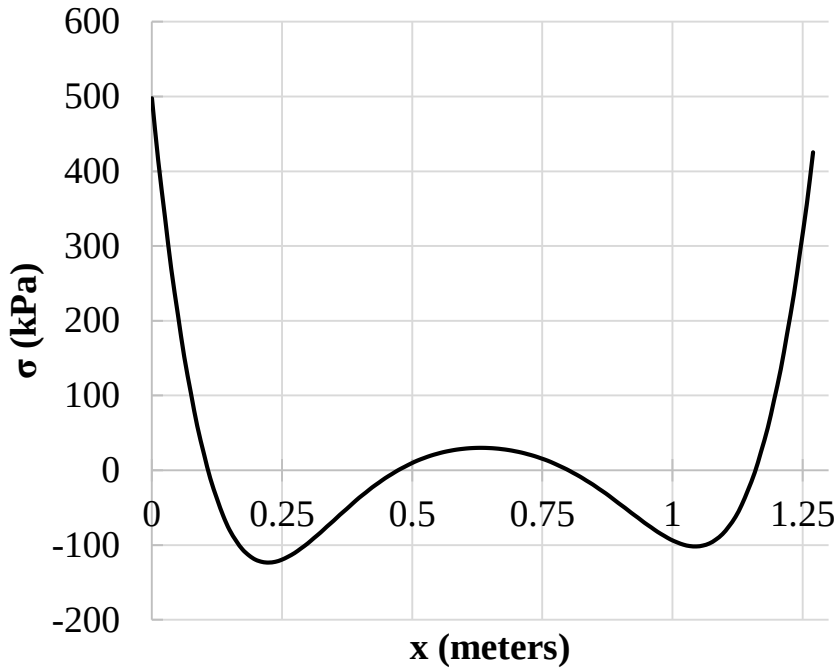

(a)

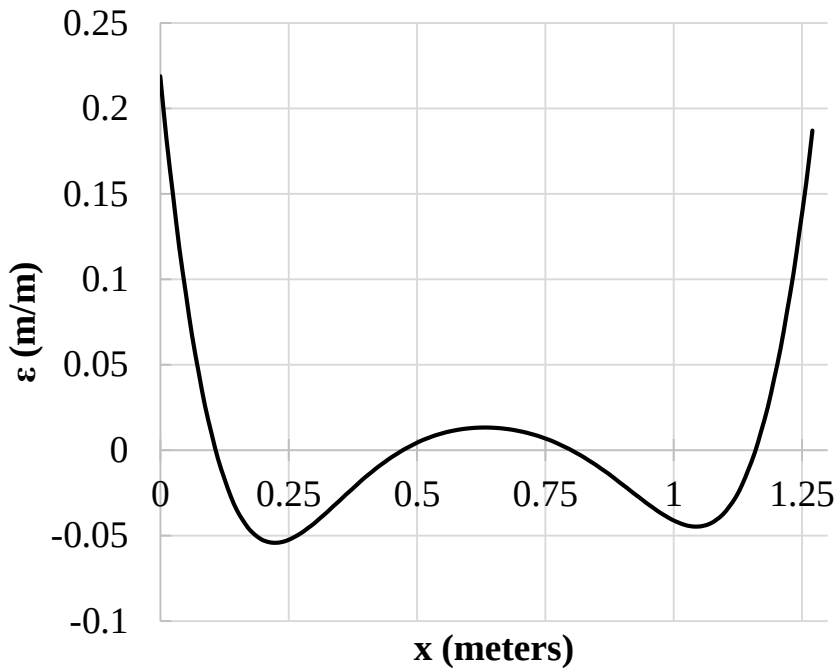

(b)

Figure 10.2 (a) Stress; and (b) strain distributions in the y-direction (Figure 9.1a) in the sealant of single sealant Model S1.

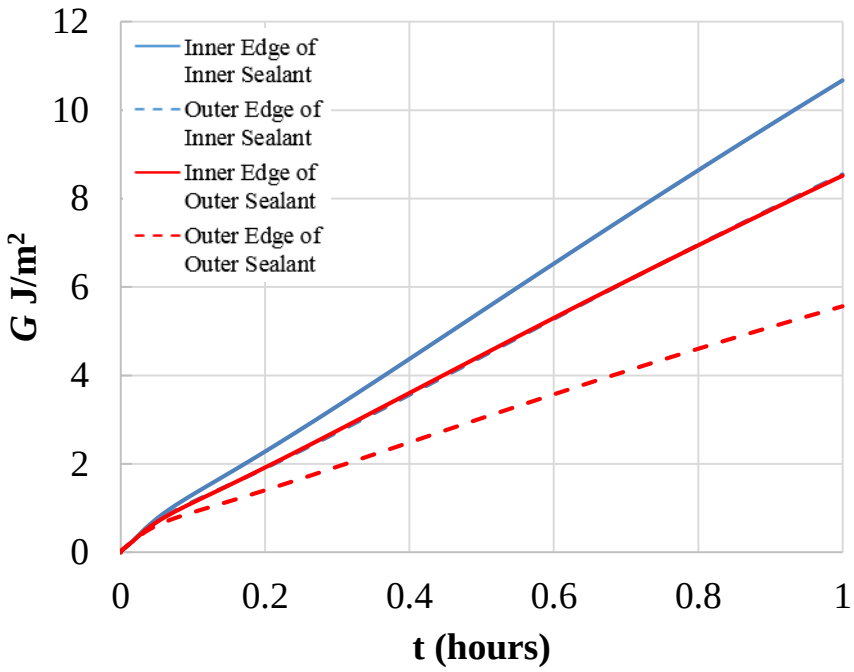

(a)

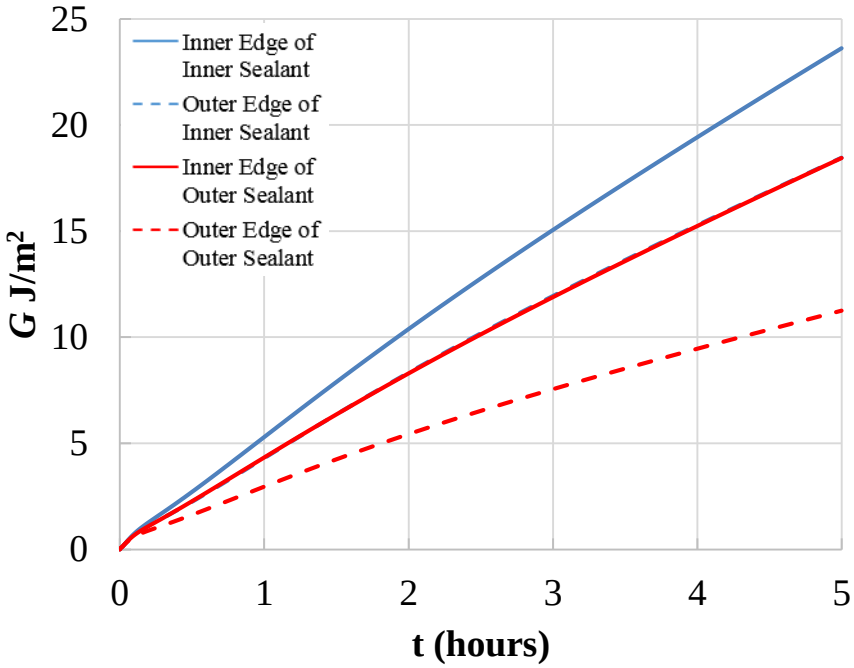

(b)

Figure 10.3 Applied energy release rate, *G*, at the inner edge of the inner sealant, the outer edge of the inner sealant, the inner edge of the inner sealant and the outer edge of the outer sealant for the duration of the simulations in (a) double sealant Model D1; and (b) double sealant Model D2.

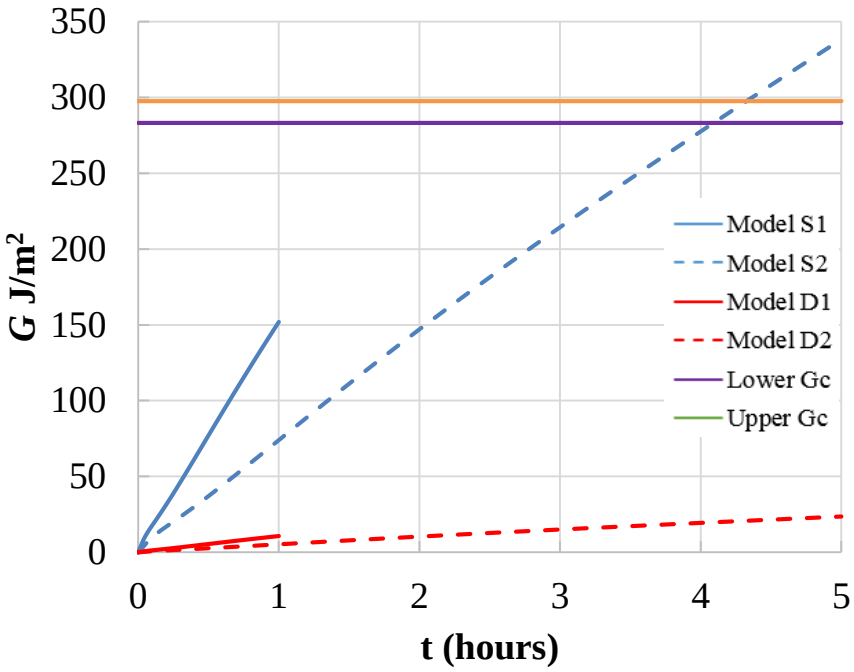

Figure 10.4 Maximum applied energy release rate, G, for the duration of simulations of Models S1, S2, D1 and D2, and the lower and upper bounds of the critical viscoelastic energy release rate, G_c.

CHAPTER 11

CONCLUSIONS TO SEALANT CHARACTERIZATION AND VISCOELASTIC SIMULATIONS

The characterization of viscoelastic properties of shingle sealant material was performed through the use of uniaxial compression testing as well as uniaxial compression creep testing at several temperatures and TTSP. Functions for the extensional viscosity were determined and used to compute the viscosities necessary to simulate the behavior of an asphalt roof shingle with one and two sealant strip for durations of 1 hour and 5 hour 150 mph 3-s hurricane gusts using the Standard Linear Solid Model and FEA. The following conclusions were drawn from experimentation and analysis.

1) The existing RSA III experimental facility is effective when used to measure the viscoelastic properties of relatively soft polymeric materials.
2) Time temperature superposition can be effectively used with data obtained from the RSA III experimental facility to determine viscoelastic properties of shingle sealant material.
3) Furthermore, TTSP can be used to significantly increase the amount of data which can be used for the derivation of viscoelastic constants.
4) The analysis predicts that the sealant strip edge closest to the nail line will fail first in both single sealant systems and double sealant systems, as the energy release rate, G, is always greater for that edge.
5) Neither the single nor double sealant asphalt shingle system will fail within one hour

of 150 mph hurricane winds.

6) From the modeling and simulations performed, it was determined that an asphalt shingle using a single sealant will fail due to 150 mph hurricane loads somewhere between 4.1 and 4.3 hours, while a roof shingle utilizing two sealant strips will last significantly longer, as shown by the energy release rate values, *G*, calculated at the edges of the sealants of the two systems. These figures are highly conservative as the model does not account for changes in applied pressures, viscosity, or cross sectional are of the sealant.

7) Based on the simulations, the an asphalt shingle with two sealant strips can be estimated to last more than 14 times longer, or over 58 hours.

CHAPTER 12

LIMITATIONS OF CURRENT STUDIES AND FUTURE WORK

It must be emphasized that the conclusions outlined above are based on the assumption that the pressures applied by the wind loading remains unchanged as the shingle sealant begins to deform under creep conditions. In actual wind-loading cases, the pressure on the portion of the shingle between the leading edge and the outer sealant will begin to increase due to sealant creep and the continued presence of high winds. Physically, this occurs due to uplift of the leading edge of the shingle, resulting in an increase in the projected area of the shingle that is exposed to existing high wind conditions. As the forces increase on the outer portion of the shingle, creep will accelerate at the outer edge of the outer sealant, resulting in a cascading set of events that ultimately lead to initial separation occurring at the outer edge of the outer sealant on the shingle. Direct visual observation of single sealant shingle failure in high winds confirms that the cascade scenario noted above indeed will lead to separation of the outer sealant.

Even though this cascading set of events was not considered in this model, it is interesting to note that the total time to separation observed in field conditions was on the order of 1.5 hours, which is the same order of magnitude as the current prediction of ~ 4 hours that does not include the pressure increase noted above. The reason for the overall qualitative agreement in time to failure between physical observations and model predictions for the single sealant system is that the rapidly accelerating cascading set of

events occurs only after sufficient sealant creep occurs to cause shingle uplift sufficient to initiate the events. This early and time-consuming portion of the creep process appears to be reasonably well predicted by the model, resulting in nominal qualitative agreement.

Based on the discussions in Chapter 10 and above, future work could include the following areas of research;

- Modifying simulations to include increasing pressure on the outer portion of the shingle as a function of uplift displacement. This could be done by using the projected area and existing bluff body equations relating the increasing force to the wind velocity. The projected area is a direct function of the displacement at the outer edge of the shingle and hence could be used to have an updated pressure as the displacement increases.
- Consider developing a more complex viscoelastic material model that would include several parameters to predict the measured response with increasing accuracy.
- Perform research to determine whether it is appropriate to quantify energy release rate under (a) nominally elastic conditions (relatively quick delamination experiments) and (b) under long term creep conditions for use in failure predictions for sealant systems.

REFERENCES

Anderson, D., D.W. Christensen, and H. Bahia (1991). "Physical Properties of Asphalt Cement and the Development of Performance Related Specifications." *Journal of the Association of Asphalt Paving Technologists*, Vol. 60, pp. 437-475.

ANSYS Inc. PDF Documentation for Release 15.0.

ASTM (2009), *Standard Test Method for Wind-Resistance of Asphalt Shingles (Fan-Induced Method) – ASTM D3161*, ASTM International, West Conshohocken, PA.

ASTM (2011), *Standard Test Method for Wind Resistance of Asphalt Shingles (Uplift Force/Uplift Resistance Method) – ASTM D7158*, ASTM International, West Conshohocken, PA.

Berdahl, P., Akbari, H., Levinson, R., and Miller, W.A. (2008). "Weathering of Roofing Materials – An Overview." *Construction and Building Materials*, 22(4), 423-433.

Chambers, R. S., Jr., E. D., Lo, C. S., Adolf, D. B., & Guess, T. R. (2000). "Micromechanical Failure Analyses for Finite Element Polymer Modeling." *Sandia National Laboratories*.

Cheng, F., Özsoy, Ö Ö, & Reddy, J. (2013). "Finite Element Modeling of Viscoelastic Behavior and Interface Damage in Adhesively Bonded Joints." *Kumar/Advances Advances in Modeling and Design of Adhesively Bonded Systems*, 23-45.

Croom, B.P., Sutton, M.A., Zhao, X., Matta, F., and Ghorbani, R. (2015a). "Modeling of Asphalt Roof Shingle-Sealant Structures for Prediction of Local Delamination under High Wind Loads." *Engineering Structures*, 96:100-110.

Croom, B.P., Sutton, M.A., Zhao, X., Matta, F., Ghorbani, R., and Aleshin, A. (2015b). Corrigendum to "Modeling of asphalt roof shingle-sealant structures for prediction of local delamination under high wind loads" [*Eng. Struct.* 96 (2015) 100–110]. In press, *Engineering Structures*.

Dixon, C.R., Masters, F.J., Prevatt, D.O., and Gurley, K.R. (2012). "An Historical Perspective on the Wind Resistance of Asphalt Shingles." *Interface*, RCI, May/June 2012, 4-14.

Dixon, C.R., Masters, F.J., Prevatt, D.O., and Gurley, K.R. (2014a). "Wind Uplift Resistance of Artificially and Naturally Aged Asphalt Shingles." *Journal of Architectural Engineering*, 20, B4014003.

Dixon, C.R., Masters, F.J., Prevatt, D.O., Gurley, K.R., Brown, T.M., Peterka, J.A., Kubena, M.E. (2014b). "The Influence of Unsealing on the Wind Resistance of Asphalt Shingles." *Journal of Wind Engineering and Industrial Aerodynamics*, 130, 30-40.

Emri, I., Gergesova, M. (2010) "Time-dependent Behavior of Solid Polymers." In *Gallegos, C. (ed.) Encyclopedia of Life Support Systems: Rheology*, pp. 247–330. EOLSS Publisher/UNESCO.

Franck, A. (2011.). "The ARES-EVF: Option for Measuring Extensional Viscosity of Polymer Melts." Retrieved from http://www.tainstruments.com/pdf/literature/APN002_ V2_ARES_ EVF_to_ measure_elongation_viscosity.pdf

Gerdeen, J. C., Lord, H. W., & Rorrer, R. A. (2006). *Engineering Design With Polymers and Composites*. Boca Raton: CRC/Taylor & Francis.

Ghorbani, R., Zhao, X., Matta, F., Sutton, M.A., Kidane, A., Liu, Z., Cope, A.D., and Reinhold, T.A. (2015). "Feasibility of Non-Contacting Measurement of Wind-Induced Full-Field Displacements on Asphalt Shingles." *Advancement of Optical Methods in Experimental Mechanics – Proc. 2014 Annual Conference on Experimental and Applied Mechanics*, Springer, New York, NY, Vol. 3, 415-421.

Kelly, P. (2015). "Linear Viscoelasticity and the Laplace Transform." In *Solid Mechanics Part I: An Introduction to Solid Mechanics*. Retrieved from http://homepages.engineering. auckland.ac.nz/~pkel015/SolidMechanicsBooks/Part_I/

Knauss, W. G. (1989) "Time Dependent Fracture of Polymers." In: *Advances in Fracture Research: Proceedings of the 7th International Conference on Fracture (ICF-7)*, Houston, Tex., 20-24 March 1989.

Liu, Z., Pogorzelski, H., Masters, F.J., Tezak, S., and Reinhold, T.A. (2010). "Surviving Nature's Fury: Performance of Asphalt Shingle Roofs in the Real World." *IBHS Disaster Safety Review*, July 2010 (reprinted in *Interface*, RCI, July 2010, 29-44).

National Roofing Contractors Association (NRCA). (2003) *The NRCA Roofing and Waterproofing Manual*, NRCA, Rosemont, IL.

Oliphant, T.E. (2006). *Guide to NumPY*. Trelgol Publishing, USA.

Peterka, J.A., Cermak, J.E., Cochran, L., Cochran, B., Hosoya, N., Derickson, R., Harper, C., Jones, J., and Metz, B. (1997). "Wind Uplift Model for Asphalt Shingles." *Journal of Architectural Engineering*, 3(4), 147-155.

Peterka, J.A., Cermak, J.E., Cochran, L., Cochran, B., Hosoya, N., Derickson, R., Harper, C., Jones, J., and Metz, B. (1999). Closure to "Wind Uplift Model for Asphalt Shingles." *Journal of Architectural Engineering*, 5(2), 68-69.

Shiao, M.L., Nester, D.A., and Terrenzio, L.A. (2003a), "On the Kinetics of Thermal Loads for Accelerated Aging," *ASTM STP 1451 – Roofing Research and Standards Development*,

T.J. Wallace and W.J. Rossiter (eds). ASTM International, West Conshohocken, PA, Vol. 5, 119-135.

Shiao, M.L., Snyder, R.A., Livsey, R.D., and Kalkanoglu, H.M. (2003b). "Measuring Uplift Resistance of Asphalt Shingles." *ASTM STP 1451 – Roofing Research and Standards Development*, T.J. Wallace and W.J. Rossiter (eds). ASTM International, West Conshohocken, PA, Vol. 5, 3-18.

Sirimamilla, P. A., Furmanski, J., & Rimnac, C. M. (2013). "Application of Viscoelastic Fracture Model and Non-uniform Crack Initiation at Clinically Relevant Notches in Crosslinked UHMWPE." *Journal of the Mechanical Behavior of Biomedical Materials, 17*, 11-21.

Sparks, P.R., Schiff, S.D., and Reinhold, T.A. (1994). "Wind Damage to Envelopes of Houses and Consequent Insurance Losses." *Journal of Wind Engineering and Industrial Aerodynamics*, 53:145-155.

Williams, M. L., Landel, R. F., & Ferry, J. D. (1955). "The Temperature Dependence of Relaxation Mechanisms in Amorphous Polymers and Other Glass-forming Liquids." *Journal of the American Chemical Society*, 77(14), 3701-3707.

Wineman, A. S., & Rajagopal, K. R. (2000). *Mechanical Response of Polymers: An Introduction*. Cambridge: Cambridge University Press.

Zhao, Y., & Kim, Y. (2003). "Time-Temperature Superposition for Asphalt Mixtures with Growing Damage and Permanent Deformation in Compression." Transportation Research Record: *Journal of the Transportation Research Board, 1832*, 161-172.

Życzkowski, M. (1991). *Creep in Structures: 4th IUTAM Symposium, Cracow, Poland, September 10-14, 1990*. Berlin: Springer-Verlag.